Direct synthesis of an iron metal-organic framework antiferromagnetic glass

Luis León-Alcaide,[a] Lucía Martínez-Goyeneche,[a] Michele Sessolo,[a] Bruno J. C. Vieira,[b] João C. Waerenborgh,[b] J. Alberto Rodríguez-Velamazán,[c] Oscar Fabelo,[c] Matthew J. Cliffe,[d] David A. Keen,[e] and Guillermo Mínguez Espallargas*[a]

[a] Instituto de Ciencia Molecular (ICMol), Universidad de Valencia, c/ Catedrático José Beltrán, 2, 46980, Paterna, Spain

[b] Centro de Ciências e Tecnologias Nucleares, DECN, Instituto Superior Técnico, Universidade de Lisboa, 2695-066 Bobadela, LRS, Portugal

[c] Institut Laue-Langevin, 6 rue Jules Horowitz, BP 156, 38042 Grenoble Cedex 9, France

[d] School of Chemistry, University of Nottingham, Nottingham NG7 2RD, United Kingdom

[e] ISIS Facility, Rutherford Appleton Laboratory, Harwell Campus, Didcot, Oxfordshire OX11 0QX, United Kingdom

Supporting Information

Contents

S1. Detailed experimental procedures

Nuclear Magnetic Resonance (NMR)

The ligand ratio was confirmed by ^{1}H NMR spectroscopy after digestion in D_2O and deuterated trifluoroacetic acid or deuterated sulfuric acid, which may cause variations in the ppm values of the signals. NMR spectra were recorded on a Bruker DRX-500 spectrometer. The molar amount of the bim^- linker (x) was determined from the singlet signals of the CH groups at position 2 of the imidazolate ring (blue for im^- and pink for bim^-).

Scanning Electron Microscopy (SEM) and Energy dispersive X-ray (EDX).

Scanning electronic micrograph images and EDX analysis were recorded in a SCIOS 2 FIB-SEM.

Polarized Light Microscopy.

Optical images were obtained with a Nikon Eclipse LV-100 Optical microscope.

CO_2 adsorption. High-pressure CO_2 adsorption isotherms (up to 15 bar) were measured using a gravimetric sorption analyzer IGA-100 (Hiden Isochema). A 50 mg sample of the adsorbent was placed in a sample holder and degassed for 2 hours at 150 ºC under vacuum. CO_2 adsorption isotherms were then acquired at 25 ºC. Equilibrium conditions were defined by a 600 s interval and a tolerance of 0.001 $mg \cdot min^{-1}$.

Single Crystal X-ray Diffraction.

A single crystal of **MUV-28** was mounted on glass fibers using a viscous hydrocarbon oil to coat the crystals and then transferred directly to the cold nitrogen stream for data collection. X-ray data were collected at 120 K on a DW rotating anode synergy R diffractometer with the (Cu-K_α) X-ray source (λ = 1. 54184 Å). Data were measured using the CrysAlisPro suite of programs.

S2. Synthesis and characterization of dg-MUV-29.

S2.1. Synthesis

All reagents were commercially available and used without further purification.

Synthesis under high-temperature conditions: Ferrocene (28 mg, 0.15 mmol) was combined with a mixture of imidazole (Him) (0.18 - 0.30 mmol) and benzimidazole (Hbim) (0 - 0.12 mmol), maintaining a total ligand amount of 0.30 mmol. The mixture was then sealed under vacuum in a layering tube with a diameter of 4 mm. The mixture was heated at 300 °C for 6 hours, yielding an orange glass. After cooling to room temperature, the layering tube was opened, and the unreacted precursors were extracted with acetonitrile, PXRD analysis revealed the formation of three distinct phases depending on the benzimidazole concentration used in the synthesis (Figure S7). When only imidazole is present ($x = 0$), the crystalline phase **MUV-24(coi)** arises, although in very low yields, with most of the material turning into a black paste that adheres to the tube and cannot be easily separated. As benzimidazole is introduced, an orange, transparent glassy monolith forms, with the formula $Fe(im)_{2-x}(bim)_x$, referred to as **dg-MUV-29-bim$_x$** (dg = direct-glass). The actual benzimidazole content in the **dg-MUV-29-bim$_x$** materials, determined by ^{1}H NMR spectroscopy (Section S2.2), closely matches the ratios of the synthetic precursors; thus, the experimental amounts will be used to denote these materials in the rest of the work.

Table S1. Applied masses and molar amounts of Him and Hbim in the reaction mixtures for the synthesis of **dg-MUV-29**. along with the *x* values used in synthesis and determined in the resulting framework (determined by ^{1}H NMR spectroscopy; see Section S2.2). * **MUV-28** cannot be isolated as a single phase following the high temperature protocol, as **dg-MUV-29** is also obtained.

Material	Initial ratio (im^- : bim^-)	Experimental ratio (im^- : bim^-)
MUV-24(coi)	2 : 0	2 : 0
dg-MUV-29	1.80 : 0.20	1.82 : 0.18
dg-MUV-29	1.60 : 0.40	1.56 : 0.44
dg-MUV-29	1.50 : 0.50	1.52 : 0.48
dg-MUV-29	1.40 : 0.60	1.40 : 0.60
MUV-28*	1.20 : 0.80	1.22 : 0.78

Throughout this section, we will use *x* to represent the found amount of benzimidazole in the framework.

S2.2. Nuclear Magnetic Resonance (NMR)

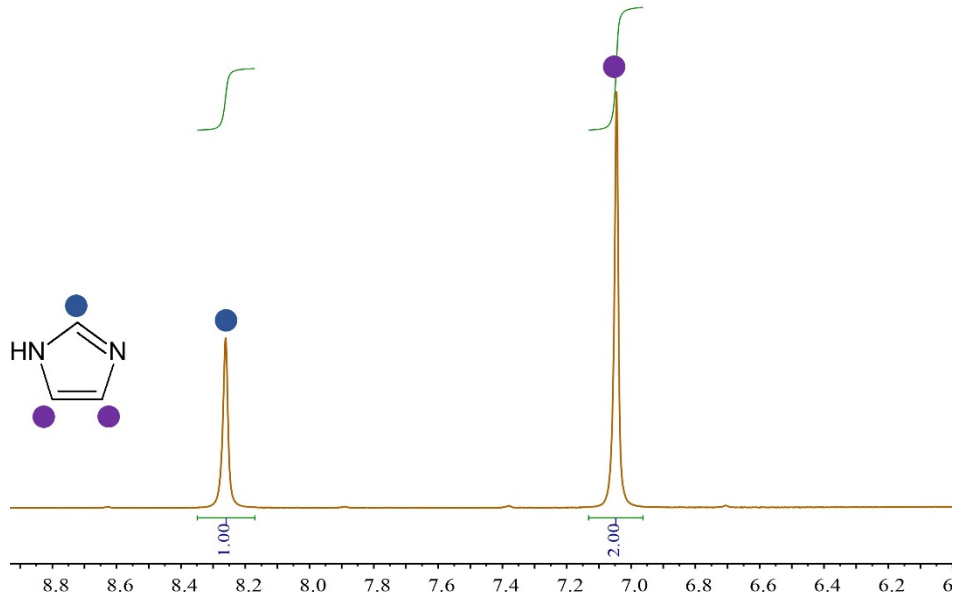

Figure S1. ^{1}H NMR spectra of the digested material with $x = 0$. Coloured circles help to localize the corresponding chemical shifts of the protons.

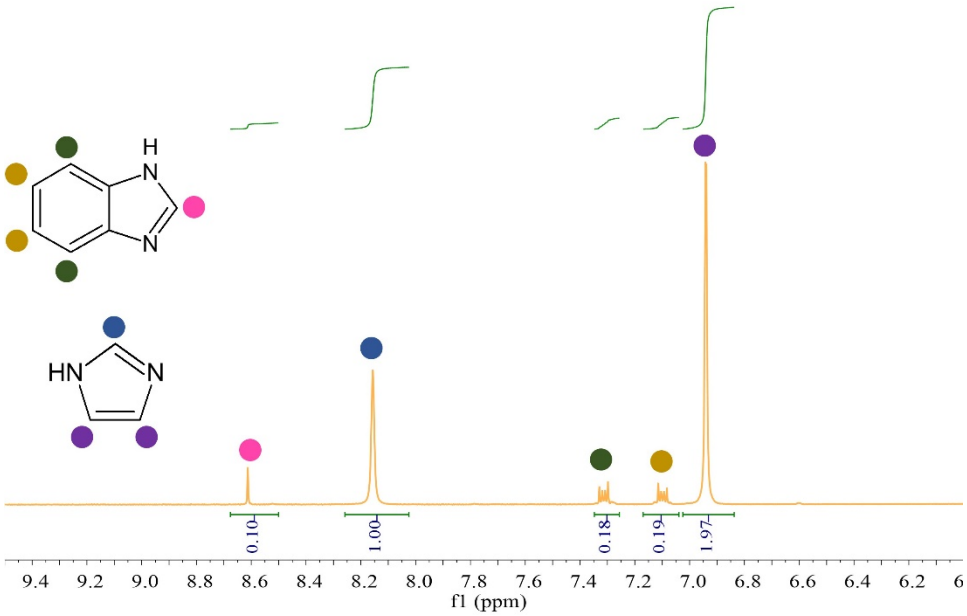

Figure S2. ^{1}H NMR spectra of the digested material with $x = 0.2$. Coloured circles help to localize the corresponding chemical shifts of the protons.

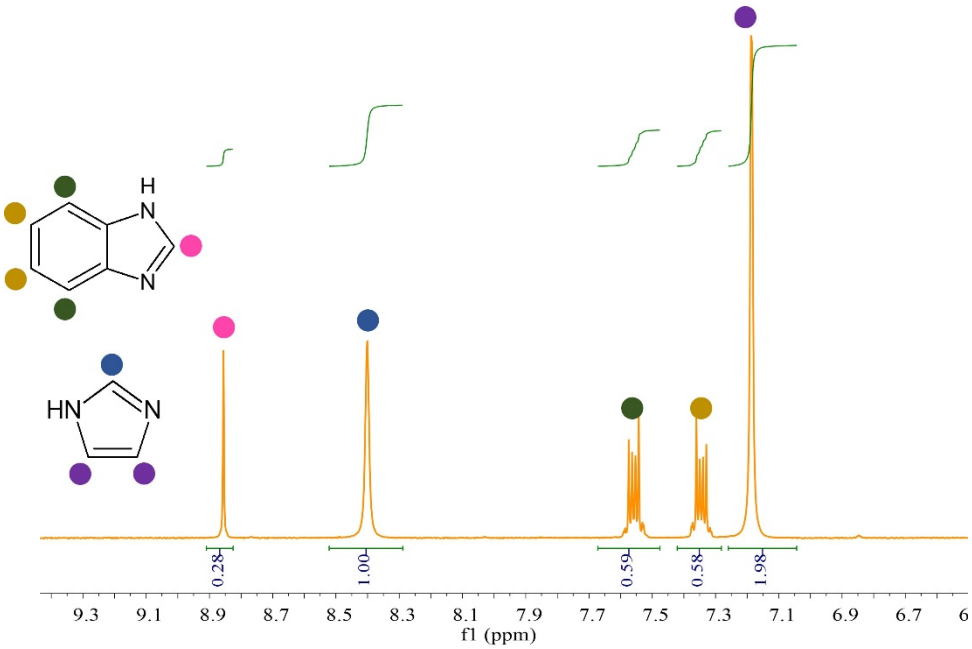

Figure S3. ^{1}H NMR spectra of the digested material with x = 0.4. Coloured circles help to localize the corresponding chemical shifts of the protons.

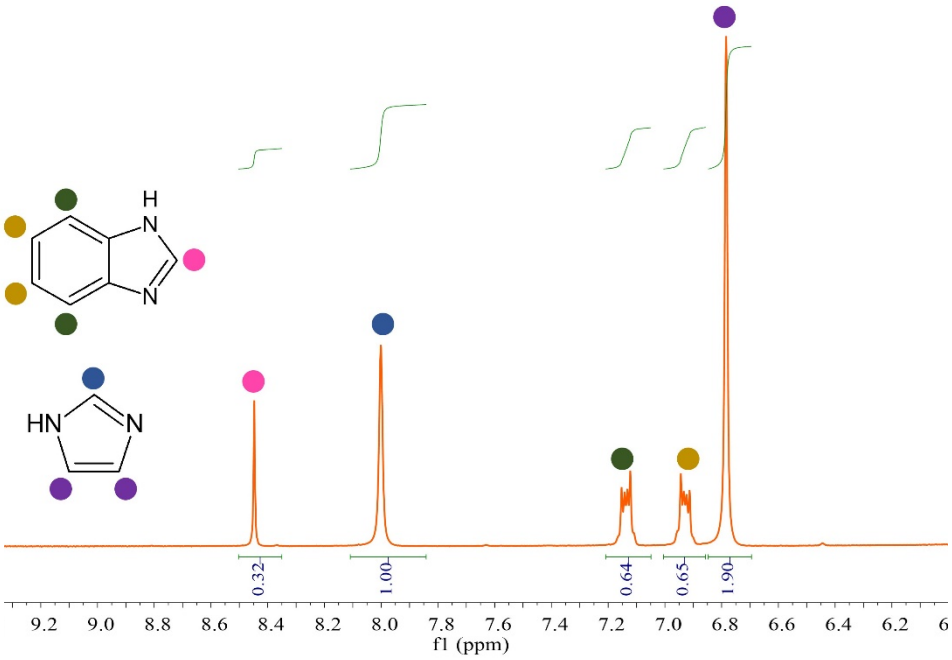

Figure S4. ^{1}H NMR spectra of the digested material with x = 0.5. Coloured circles help to localize the corresponding chemical shifts of the protons.

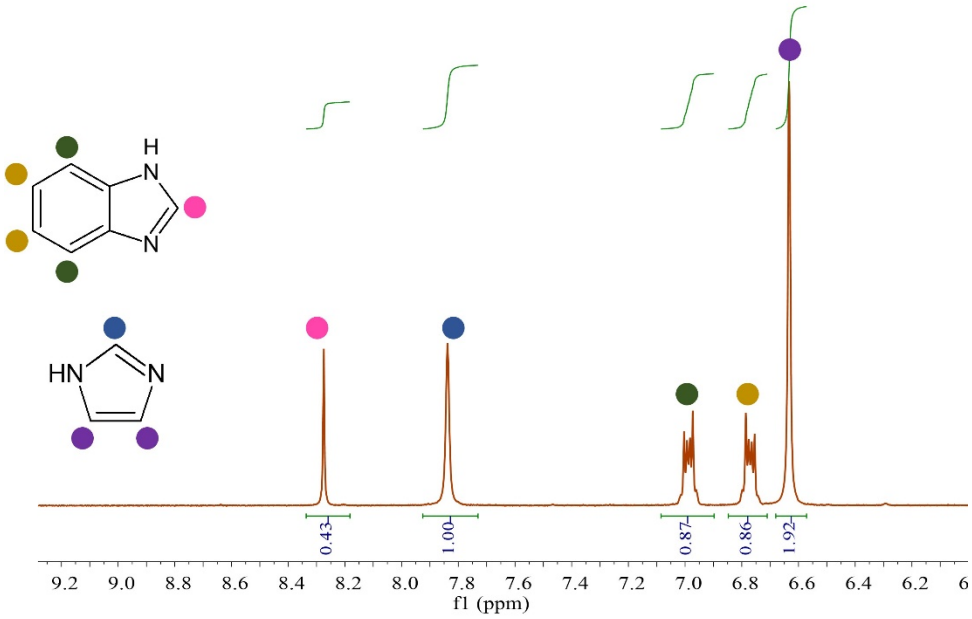

Figure S5. ^{1}H NMR spectra of the digested material with x = 0.6. Coloured circles help to localize the corresponding chemical shifts of the protons.

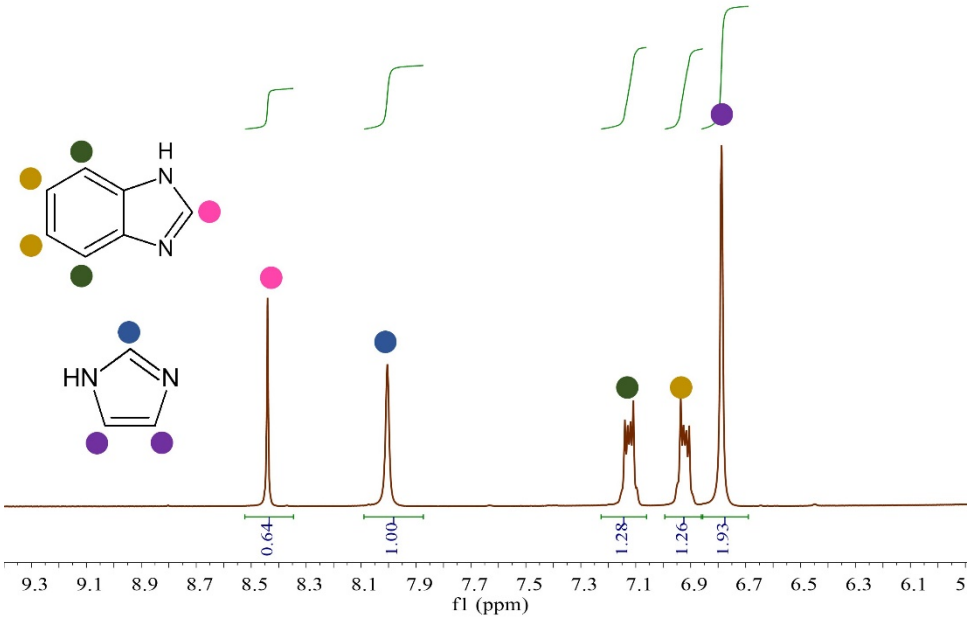

Figure S6. ^{1}H NMR spectra of the digested material with x = 0.8. Coloured circles help to localize the corresponding chemical shifts of the protons.

S2.3. X-Ray Powder Diffraction

All materials were characterized by X-ray powder diffraction. Three distinct phases were identified based on the proportions of the precursors Him and Hbim. The addition of only Him resulted in the phase known as **MUV-24(coi)** ($Fe(im)_2$), previously reported as a phase formed during the heating of **IMIDFE**. Upon introducing Hbim, an amorphous phase composed of $Fe(im)_x(bim)_{2-x}$, referred to as **dg-MUV-29**, emerges. In this phase we cannot observe any Bragg diffraction. Further increases in Hbim concentration as a ligand led to the appearance of again, a crystalline phase that corresponds with the **MUV-28**. It is important to note that for x = 0.8, the **MUV-28** appears together with **dg-MUV-29**; the latter is not detectable by X-ray powder diffraction but can be observed visually.

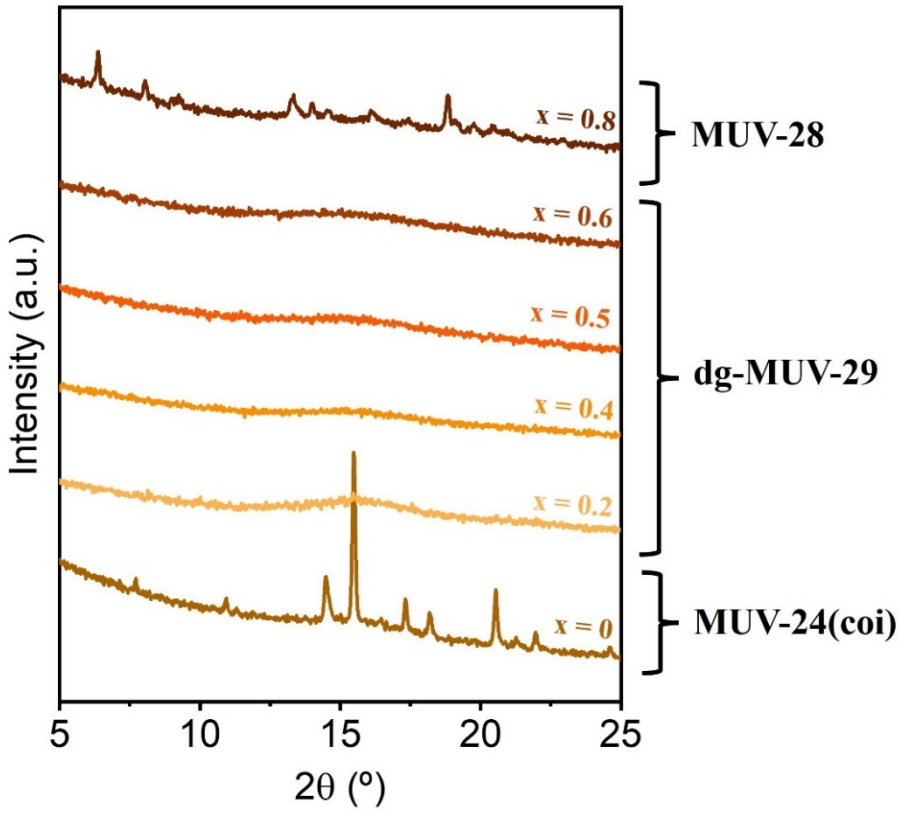

Figure S7. X-ray powder diffraction of the phases formed by varying molar amounts of Him and Hbim in the reaction mixtures, leading to the formation of **MUV-24-coi**, **dg-MUV-29**, and **MUV-28**. The x values correspond to the amount of benzimidazole determined by ^{1}H NMR spectroscopy; see Section S2.2.

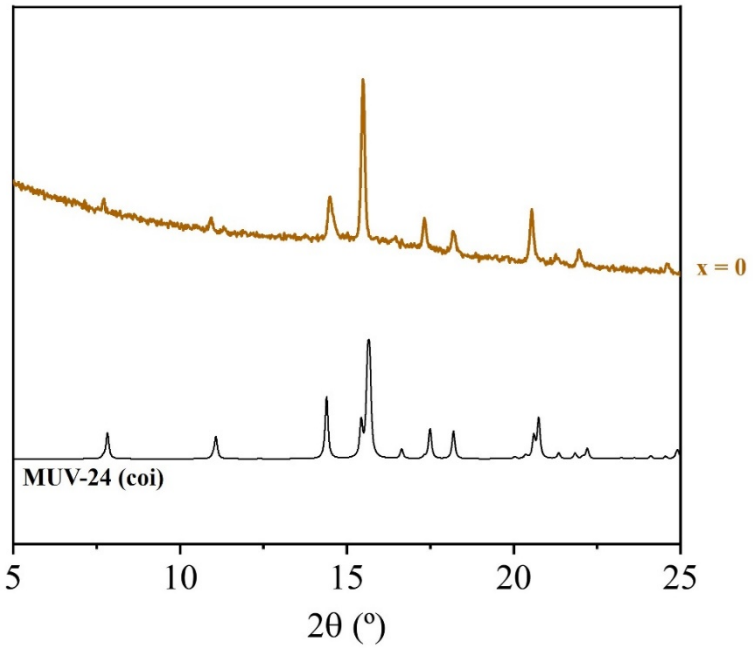

Figure S8. X-ray powder diffraction of $x = 0$ compared with the theoretical pattern of **MUV-24 (coi)**. It is important to note that the discrepancies between the theoretical and experimental results are primarily attributed to the low quality of the crystals.

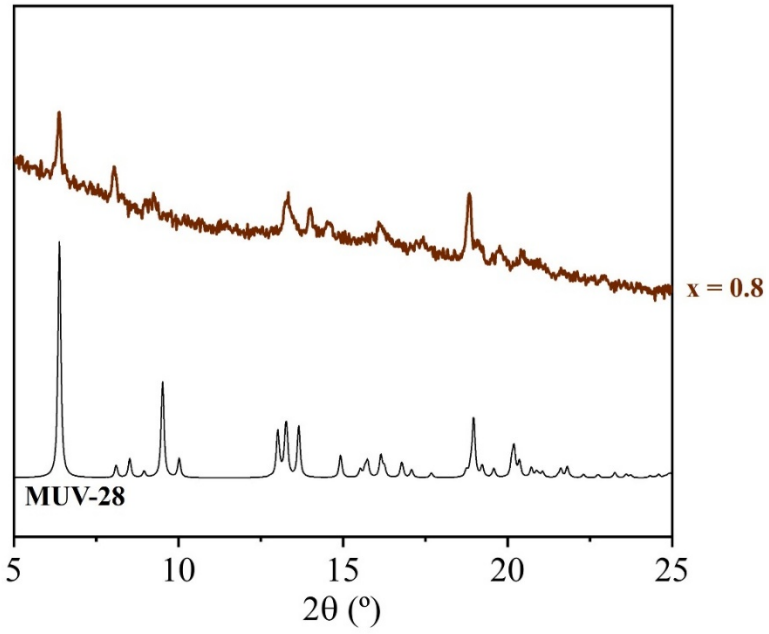

Figure S9. X-ray powder diffraction of $x = 0.8$ compared with the theoretical pattern of **MUV-28**. It is important to note that the discrepancies between the theoretical and experimental results are primarily attributed to the low quality of the crystals.

S2.4. Differential Scanning Calorimetry (DSC)

Thermal analysis was performed using coupled thermogravimetric analysis and differential scanning calorimetry (TGA/DSC) under an N_2 atmosphere at a heating rate of ±10 °C·min^{-1} (Figure S10). The study focused on the **dg-MUV-29** family, with **dg-MUV-29-bim$_{0.48}$** serving as a representative example. The results showed no endothermic signal corresponding to framework melting. Instead, they revealed the characteristic glass transition (T_g), defined as the onset temperature of the endothermic calorimetric signal, confirming the material's glassy nature. After the T_g, continued heating leads to the material's decomposition at 440 ºC. To investigate the effect of benzimidazole on the melting process, various DSC measurements were conducted on different members of the **dg-MUV-29** family, along with **MUV-24(coi)**, **a$_g$-MUV-24**, and the sample prepared with $x = 0.80$, which predominantly consists of **dg-MUV-29** with some crystalline **MUV-28** present (Figure S11). The DSC measurements were performed after activating the sample at 250 ºC to remove any unreacted precursors. For **MUV-24(coi)**, no signal corresponding to a T_g is detected, which is consistent with expectations. The T_g ranges from 225 ºC to 250 ºC for **dg-MUV-29-bim$_{0.18}$** to **dg-MUV-29-bim$_{0.60}$**, slightly superior to the reported for MQ **a$_g$-MUV-24** (T_g = 192 ºC). This effect is consistent with previous observations for the Zn analogue were T_g also depends on x and slightly increases with bim$^-$ concentration. It is remarkable that when the amount of x is increased more than 0.60, the glass transition temperature remains constant. This indicates that a different phase is formed when x is increased beyond this point (**MUV-28**), suggesting that the glassy framework cannot incorporate more than this amount of benzimidazole. This phase segregation was also corroborated by PXRD diffraction. In the first upscan for pure imidazole (**MUV-24(coi)**), ligand discoordination is observed, which is consistent with the behavior expected in a crystalline phase. However, in the second upscan (as shown in Figure S10), no endothermic signal associated with the glass transition is detected. Importantly, in the family of **dg-MUV-29** the glass transition is reversible, allowing for multiple cycles without any alteration (Figure S12). We also present the signal of the material without the activation process, where the glass transition is more difficult to establish due to the broadening of the peak.

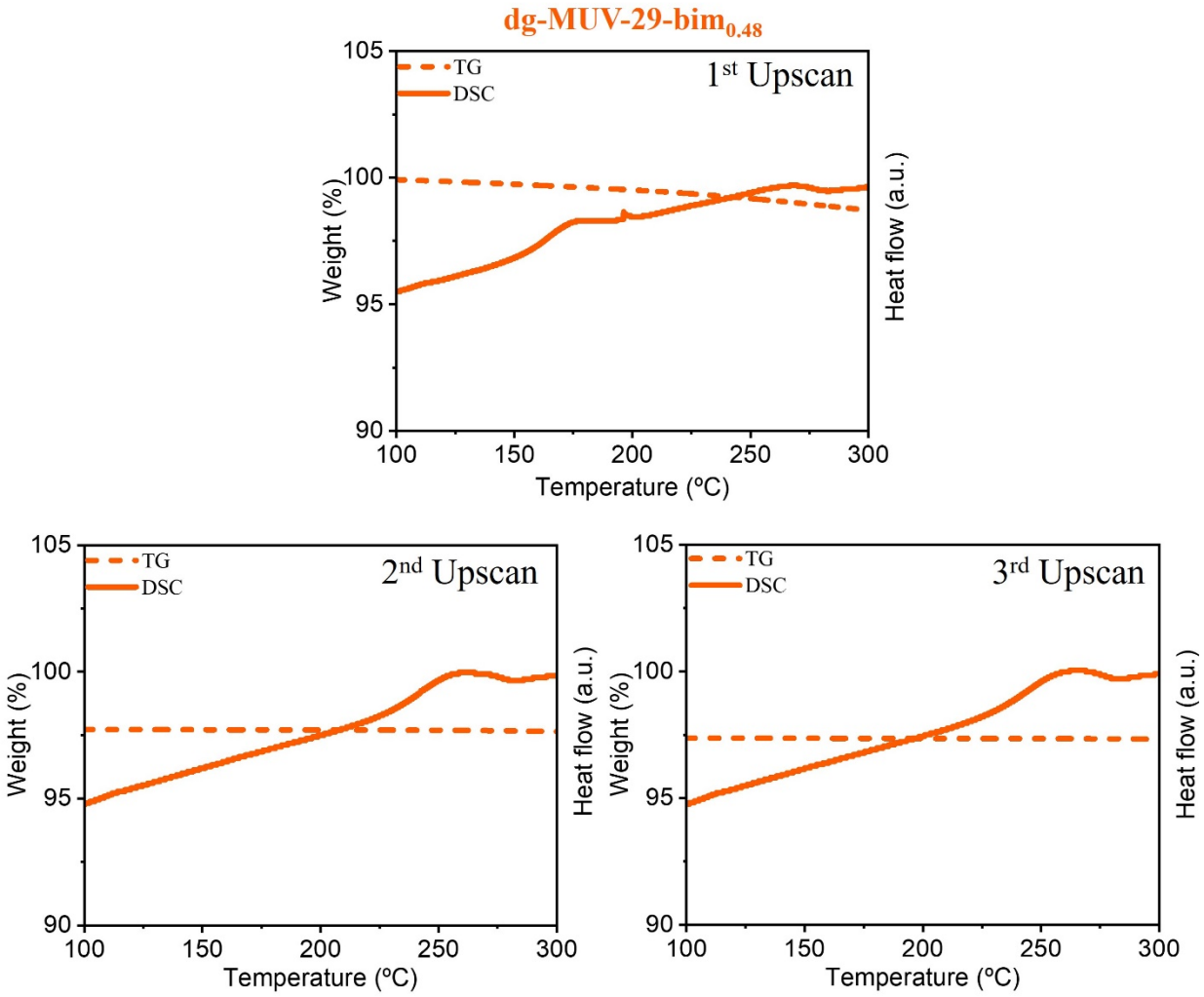

Figure S10. Successive cycles of thermogravimetric analysis (in dark red) coupled with differential scanning calorimetry (in orange) of **dg-MUV-29-bim$_{0.48}$**, demonstrate the mass loss and phase transitions. The first upscan corresponds to the activation process and is accompanied by a slight mass loss. The second and third scans do not show any significant mass loss associated with the T_g.

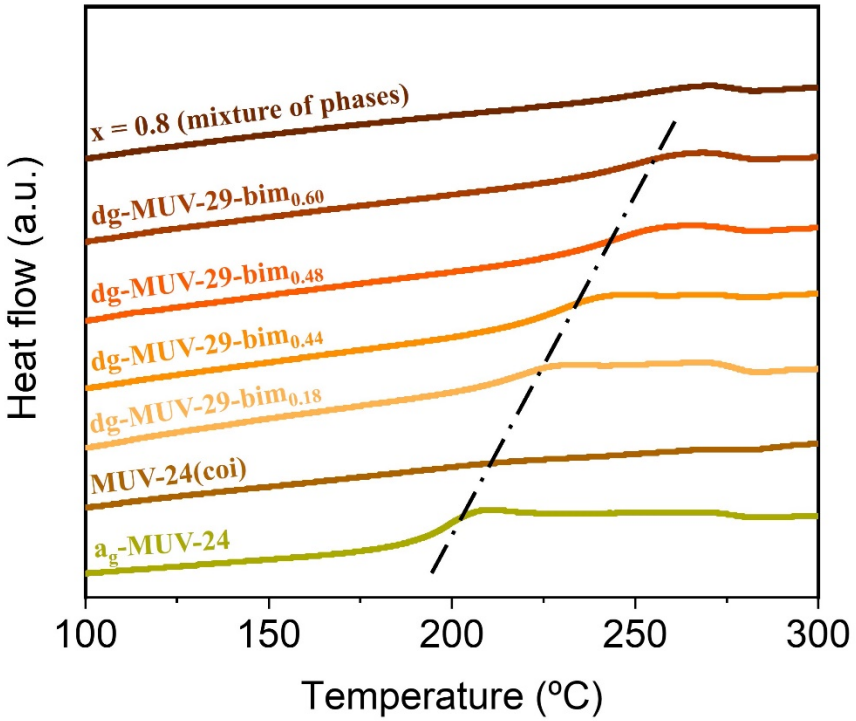

Material	Glass transition (ºC)
x = 0.8 (mixture of phases)	245
dg-MUV-29-bim$_{0.60}$	244
dg-MUV-29-bim$_{0.48}$	227
dg-MUV-29-bim$_{0.44}$	216
dg-MUV-29-bim$_{0.18}$	208
MUV-24(coi)	-
a$_g$-MUV-24	192

Figure S11. Top: DSC first upscan of the materials with $0 < x > 0.78$ (higher x values exhibit a crystalline impurity and are also adhered to the synthetic reactor). An increase in the glass transition temperature (T_g) is observed with the addition of benzimidazole. Below: Table showing the glass transition values.

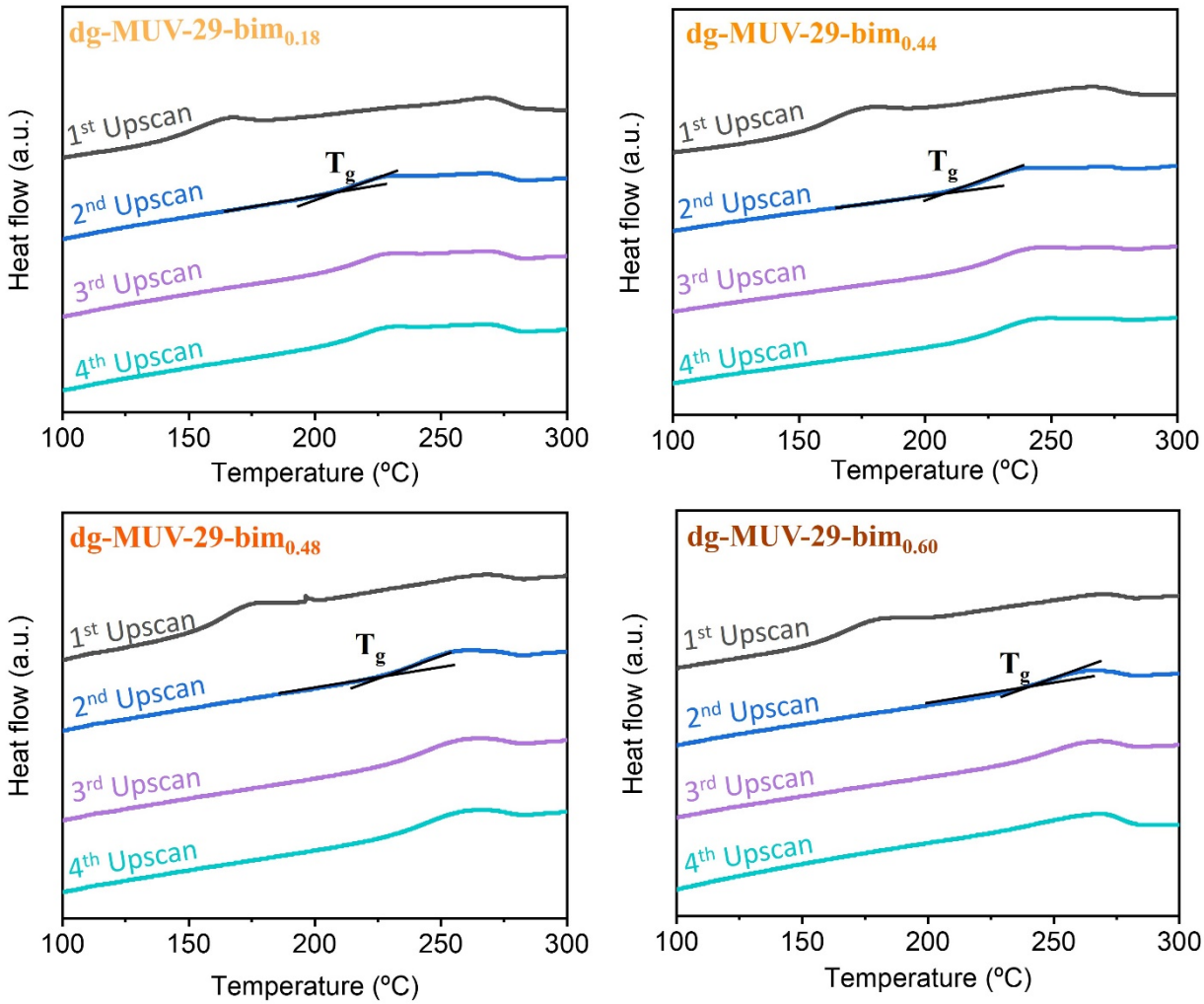

Figure S12. Successive DSC upscans of the **dg-MUV-29** family reveal a less defined step in the first upscan, corresponding to the activation of the material with the removal of some ligand molecules from the framework. The subsequent upscans demonstrate that the T_g is reversible, and the material remains stable throughout all cycles. The T_g intersection is shown only in the second upscan, as in the first upscan the transition is obscured by impurities. It is not displayed in the subsequent upscans to clearly demonstrate that the glass transition is maintained throughout the cycles.

S2.5. X-ray Total Scattering

The lack of long-range order in the glasses is confirmed by the absence of sharp features in their X-ray total scattering data (Figure S13). Pair distribution functions (PDF or $D(r)$) for **dg-MUV-29-bim$_{0.18}$** and **dg- MUV-29-bim$_{0.48}$** were extracted from the total scattering data via appropriate corrections and subsequent Fourier transformation and are presented in Figure S14. This data was compared with crystalline **IMIDFE** and MQ **a$_g$-MUV-24**. The short-range correlations are similar, except for the appearance of a peak at 2.44 Å in the **dg-MUV-29** family, corresponding to the distance between carbon atoms in the benzene ring of benzimidazole, and extending up to approximately 6 Å, which matches the distance between neighboring Fe^{II} centers. This clearly indicates that the tetrahedral coordination of the Fe^{II} centers with imidazolate linkers is maintained in **dg-MUV-29** materials, and that their chemical environment is similar to that of MQ **a$_g$-MUV-24**. However, additional Bragg peaks were observed in the MQ **a$_g$-MUV-24** data at higher Q values (Figure S16). These peaks were attributed to crystalline impurities of Al and Fe_2N, that avoid the study of the magnetic properties of these materials.[1]

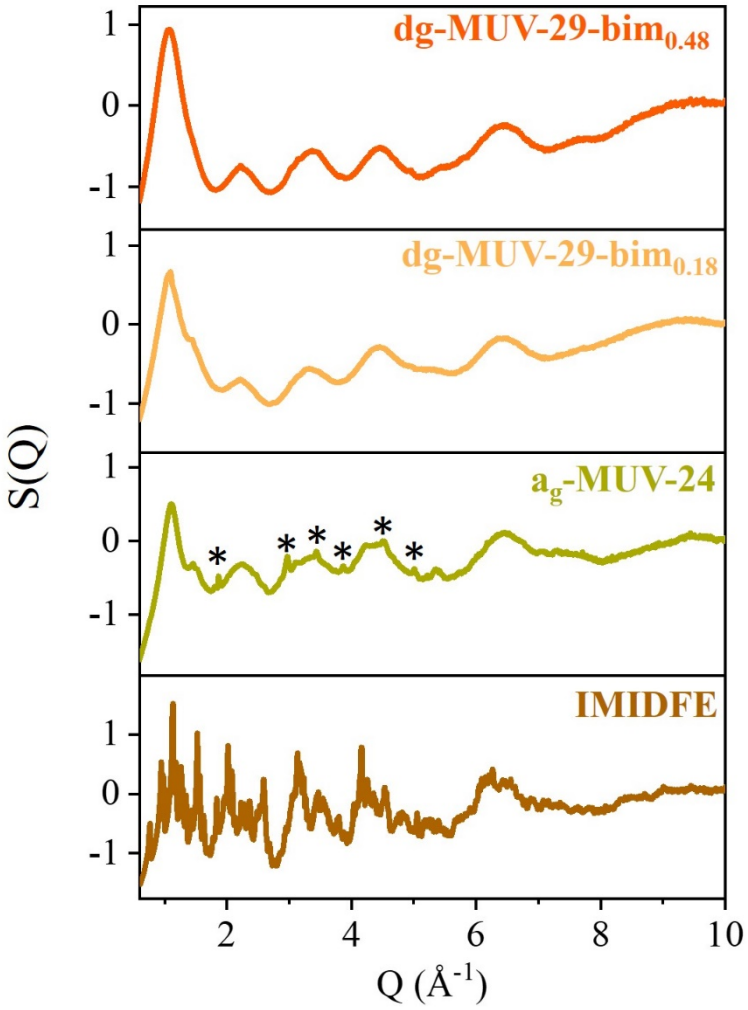

Figure S13. Total scattering factors, *S*(Q), of **Fe(im)$_2$**, **a$_g$-MUV-24**, **dg-MUV-29-bim$_{0.18}$** and **dg-MUV-29-bim$_{0.48}$.** * These peaks are attributed to Al from the pan and Fe_2N, indicating partial decomposition of the material in the case of **a$_g$-MUV-24**. It is evident that there is an increase in phase purity of **dg-MUV-29**, as no peaks associated with phase impurities are observed.

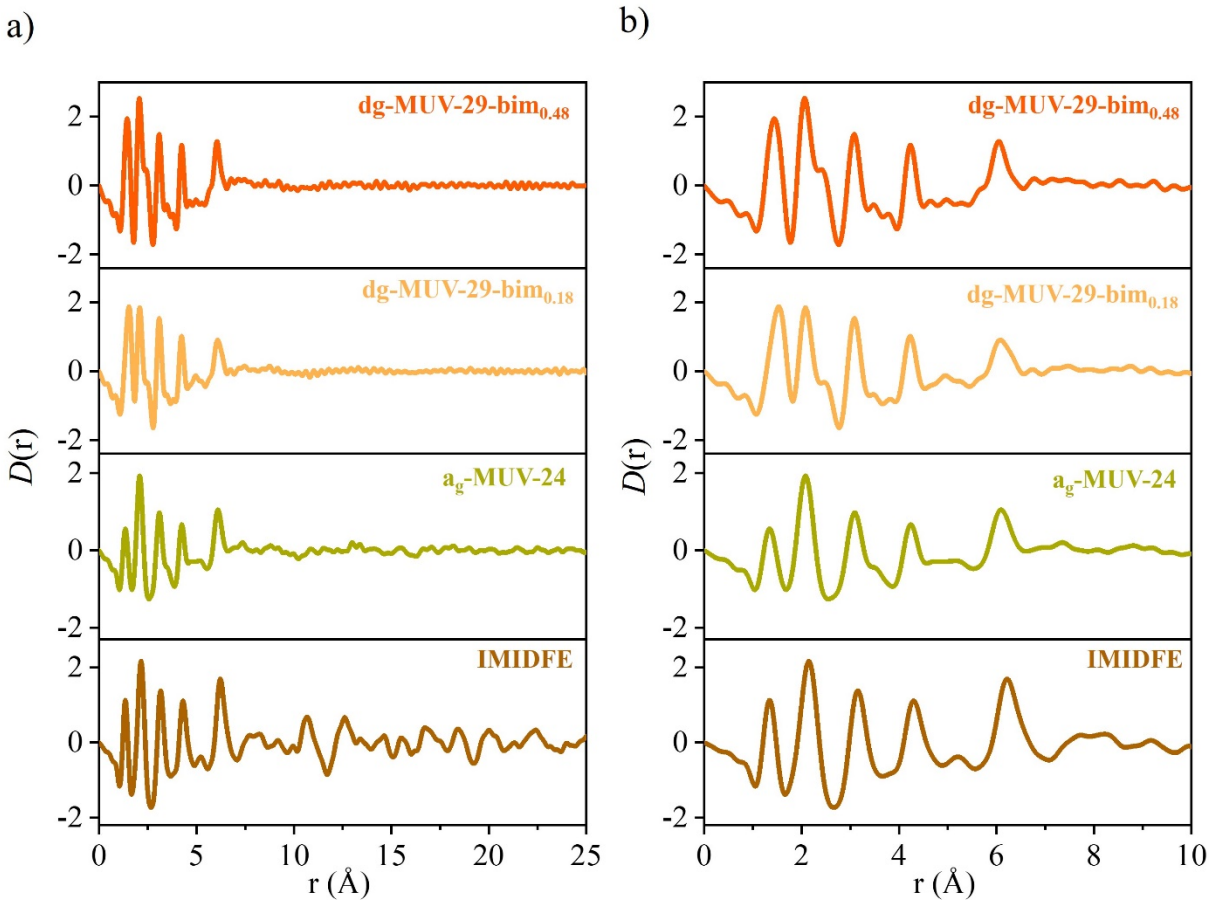

Figure S14. XPDF in the form of *D*(*r*) of **Fe(im)$_2$**, **a$_g$-MUV-24**, **dg-MUV-29-bim$_{0.12}$** and **dg-MUV-29-bim$_{0.48}$.**

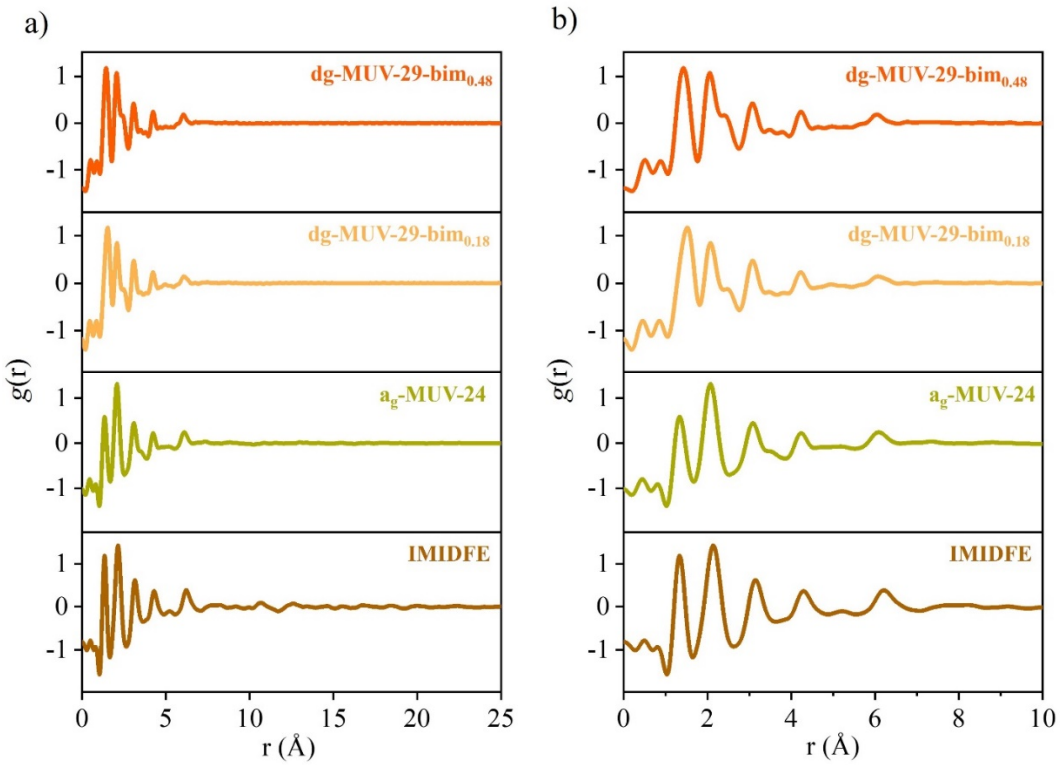

Figure S15. XPDF in the form of $g(r)$ of **Fe(im)$_2$**, **a$_g$-MUV-24**, **dg-MUV-29-bim$_{0.12}$** and **dg-MUV-29-bim$_{0.48}$.**

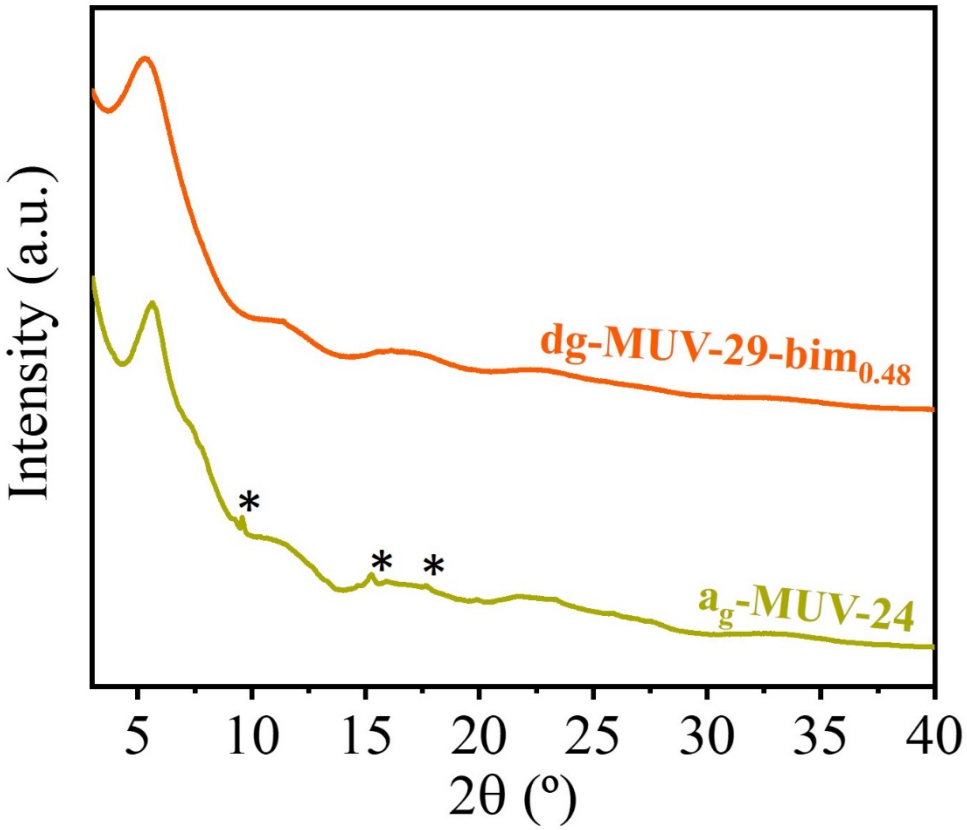

Figure S16. Comparison of the glasses **a_g-MUV-24** and **dg-MUV-29-bim$_{0.48}$**, produced via melt-quenching and direct-glass synthesis methods, respectively, reveals that the crystalline impurities in the **a_g-MUV-24** generated through melt quenching are not present in the **dg-MUV-29-bim$_{0.48}$**. * These impurities, identified as Fe_2N due to partial decomposition of the material, are further corroborated by Mössbauer spectroscopy.

S2.6. Polarized Light Microscopy

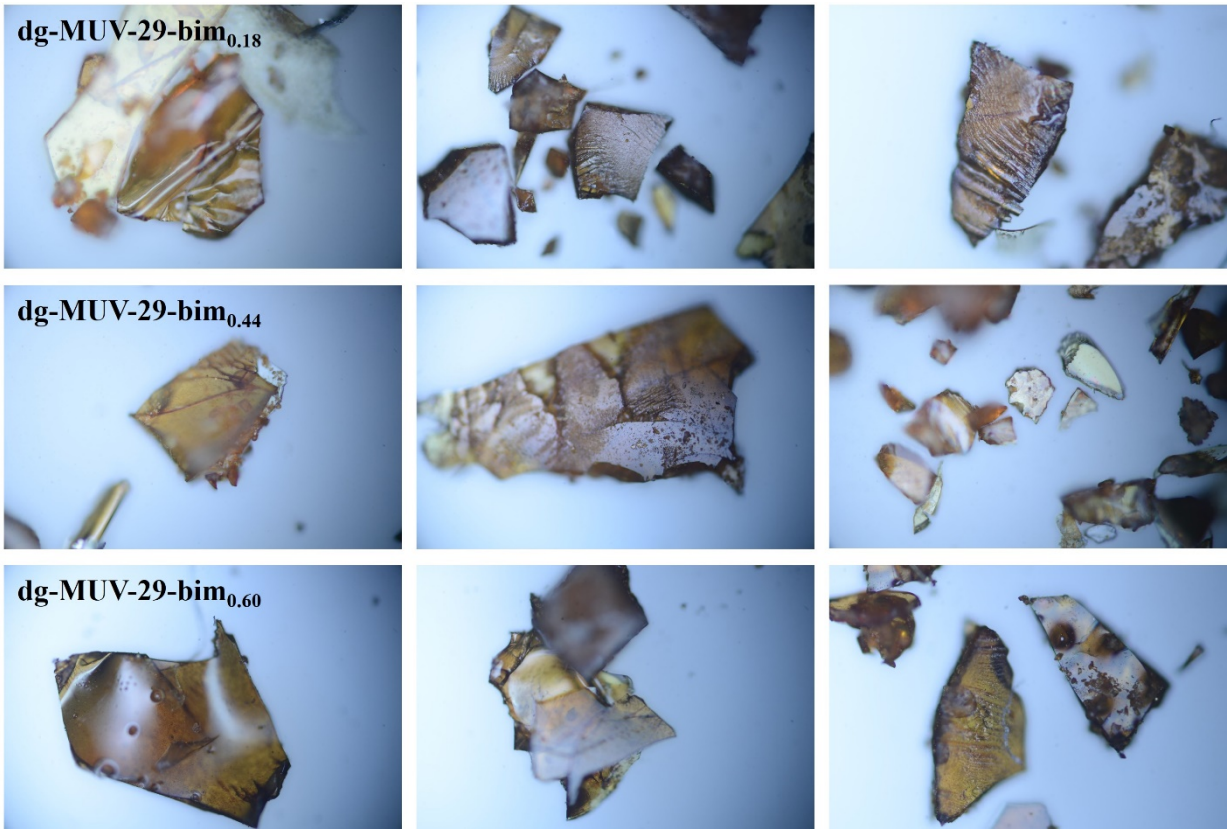

Figure S17. Optical images of different **dg-MUV-29** monolithic glass

S2.7. Scanning Electron Microscopy (SEM) and Energy Dispersive X-ray (EDX)

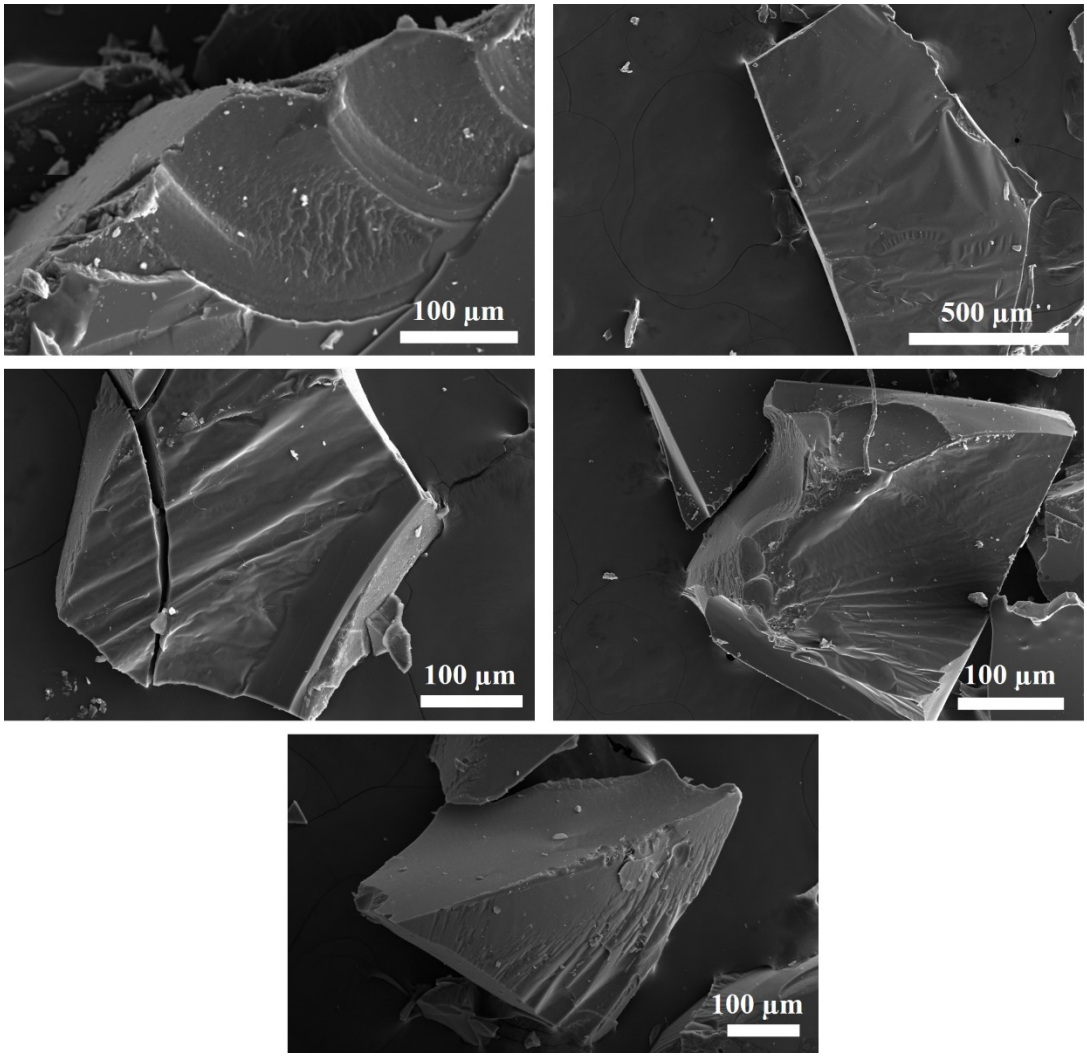

Figure S18. SEM images of **dg-MUV-29** glassy monoliths.

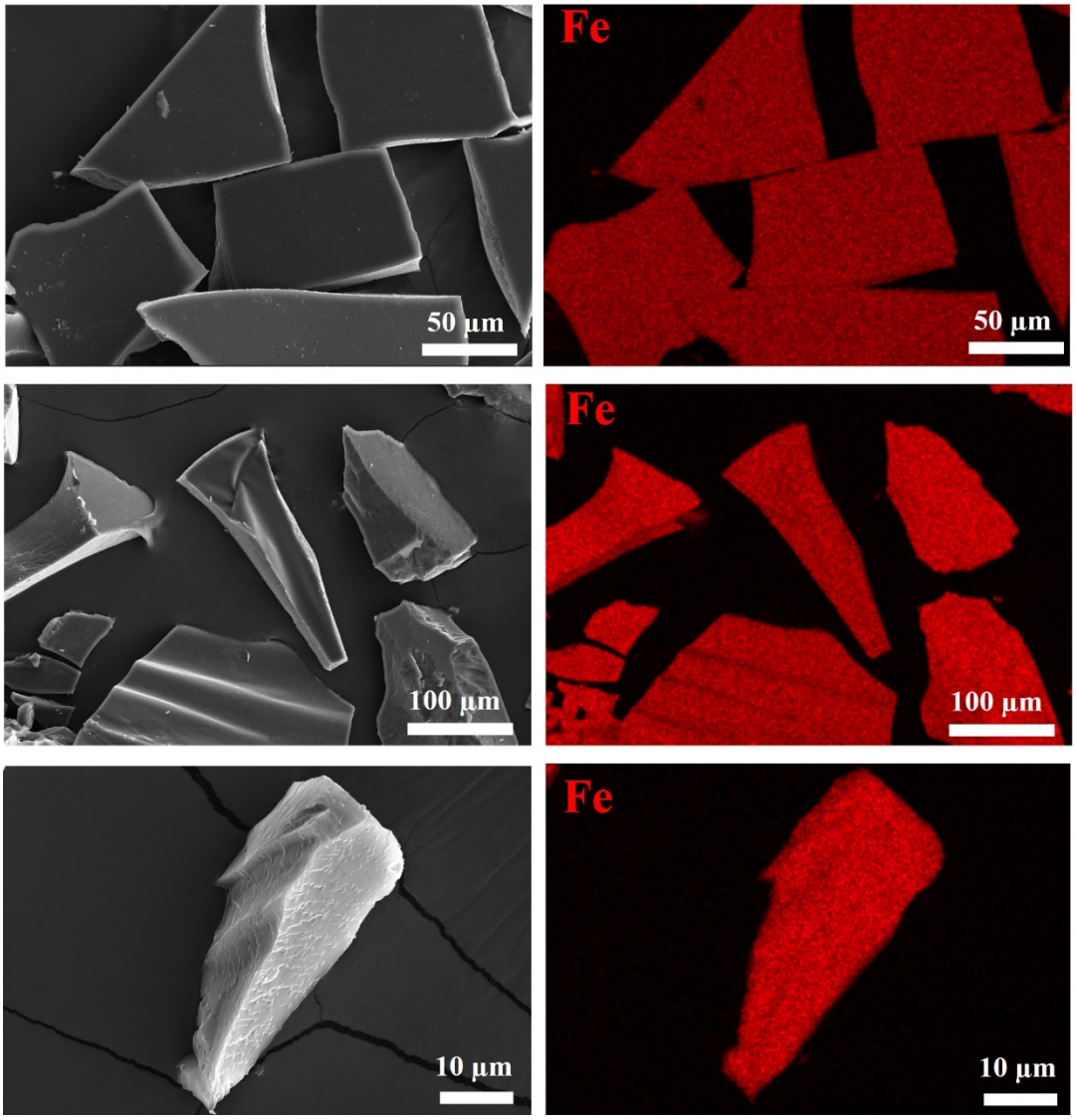

Figure S19. SEM and EDX mapping of **dg-MUV-29**.

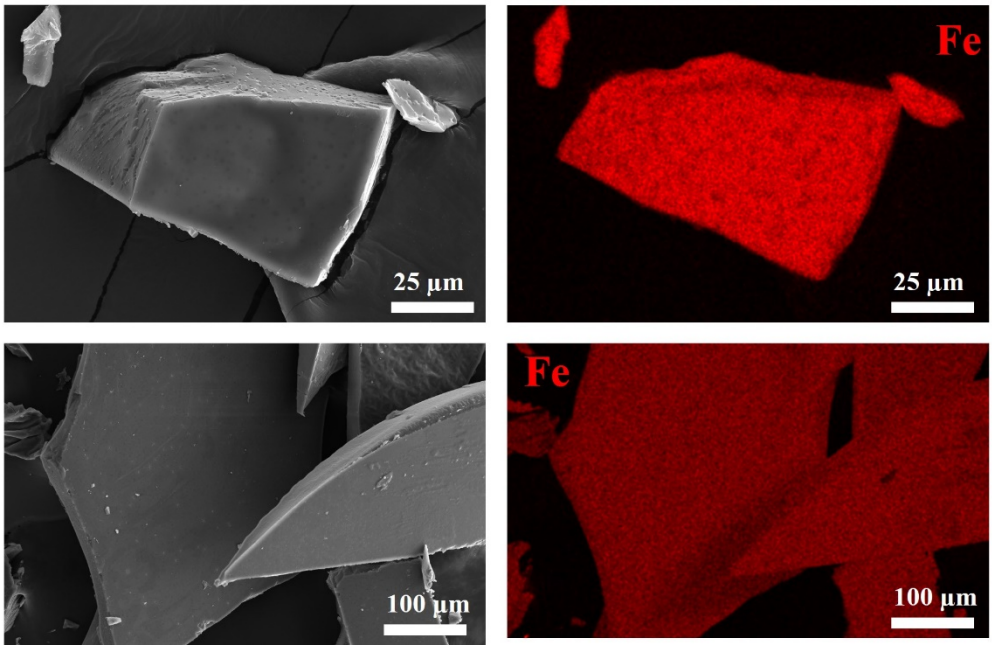

Figure S20. SEM and EDX mapping of **dg-MUV-29.**

S2.8. Mössbauer Spectroscopy

The spectrum of **IMIDFE** consists of two quadrupole doublets. The estimated isomer shifts are typical of high-spin Fe^{II} (electronic state S=2).[2] The doublet with lower isomer shift, IS, is consistent with Fe^{II} in tetrahedral coordination while the doublet with higher IS with Fe^{II} in octahedral coordination. In the crystalline samples, therefore, approximately two thirds of the Fe^{II} cations are on tetrahedral sites and one third on octahedral sites in agreement with crystallographic data reported for **IMIDFE** [3].

In the **a_g-MUV-24** the main phase incorporating ~97% of the total Fe in the sample, contains only Fe^{II} tetrahedrally coordinated. The peaks are broader than in the case of **IMIDFE.** They have the same relative area but different widths, revealing an unresolved distribution of slightly different tetrahedral sites, typical of amorphous materials where Fe cations have the same coordination number but are located on sites with little different geometries and environments, leading to slightly different IS and quadrupole splittings, QS. In the present case, more distorted sites, with higher QS, also have higher IS. No octahedrally coordinated Fe^{II} is detected. A very low intensity sextet is also observed, corresponding to ~3% of the Fe in the sample, which may be attributed to an iron nitride impurity.[4]

The **dg-MUV-29** spectrum shows broad peaks similar to those observed for **a_g-MUV-24**, typical of an amorphous material. The spectrum is therefore fitted with a distribution of QS. The average IS is consistent with tetrahedral coordination of all Fe^{II} cations as in **a_g-MUV-24**. [9] No impurity phase is detected in **dg-MUV-29** sample.

Table S2. Estimated parameters from the Mössbauer spectra of the **IMIDFE**, **a_g-MUV-24** and **dg-MUV-29** samples taken at 80K.

	IS mm/s	ε, QS mms^{-1}	B_{hf} tesla	Γ mm/s	I	
IMIDFE	0.92	2.55	-	0.31	65%	**Fe^{II} CN=4**
	1.09	1.89	-	0.26	35%	**Fe^{II} CN=6**
a_g-MUV-24	0.89	2.86	-	dist	97%	**Fe^{II} CN=4**
	0.41	0.07	24.7	0.26	3%	**Fe nitride**
dg-MUV-29	0.85	2.82	-	dist	100%	**Fe^{II} CN=4**

IS isomer shift relative to metallic α-Fe at 298 K. QS (mm/s) quadrupole splitting and $\varepsilon = (e^2QVzz/4)(3\cos^2\theta - 1)$ quadrupole shift estimated for quadrupole doublets and magnetic sextets, respectively. (In the case of distributions, dist, IS and QS correspond to the average values). B_{hf} magnetic hyperfine field. Γ peak width. I relative area. CN coordination number. Estimated errors ≤ 0.02 mm/s for IS, ε, Γ, < 0.2 T for B_{hf} and < 2% for I.

The spectra of the **dg-MUV-29** sample collected between 20 K and 100 K are similar, showing two broad peaks with the same relative area but different widths. As explained above this is characteristic of amorphous materials. The spectra were therefore fitted with a distribution of QS. The average IS is consistent with tetrahedral coordination of all Fe^{II} cations, similar to that in the crystalline **IMIDFE**. The temperature dependence of the average QS is attributed to the population of excited electronic states. When the ground and first excited electronic states for high-spin Fe^{II} are separated by an energy on the order of thermal energy (0-500 K), the QS decreases with increasing temperature as the excited states are populated.

At 4 K, a magnetic hyperfine splitting is observed, indicating strong magnetic correlations in agreement with the magnetic transition seen in magnetization data. The shape of the magnetically split signal for Fe^{II} reveals that the quadrupole hyperfine interactions are not negligible compared to the magnetic hyperfine interactions. Consequently, the hyperfine Hamiltonian must be solved to determine the peak positions and intensities, which depend on parameters such as the quadrupole interaction $\Delta = 1/2(e^2QV_{zz})$, the asymmetry parameter of the electric field gradient (η), and the angles θ (between the magnetic hyperfine field, B_{hf}, and the principal axis of the electric field gradient, V_{zz}) and φ (between V_{xx} and the projection of B_{hf} on the *xy* plane). In the amorphous phase of the **dg-MUV-29**, the Fe^{II} sites vary slightly from each other, resulting in distributions of B_{hf}, Δ, η, θ, and φ. The large number of fitting parameters makes it impractical to use an accurate non-linear least-squares fitting method. Therefore, following the approach of Ruebenbauer and Birchall,[5] several simulated spectra were generated, each assuming single values for the mentioned parameters. The best match was achieved with the following values: B_{hf} = 15 T, Δ = -2.42 mm s^{-1}, η = 0.70, θ = 70º, φ = 120º, and IS = 0.90 mm s^{-1}. These can be considered average values for the distributions.

The key parameters for characterizing the **dg-MUV-29** include the magnitude of B_{hf}, which is consistent with a spin state of S = 2 and a significant orbital magnetic moment. The IS values are also in line with those derived at 20 K and higher temperatures, indicating four-coordinated high-spin Fe^{II}. The increase in IS with decreasing temperature is explained by the second-order Doppler shift.

Table S3. Estimated parameters from Mössbauer spectra of **dg-MUV-29** at different temperatures.

Temperature (K)	IS mm s^{-1}	ε, QS mm s^{-1}
100	0.86	2.66
80	0.85	2.68
60	0.87	2.77
40	0.88	2.82
20	0.88	2.88

IS average isomer shift relative to metallic α-Fe at 298 K. QS (mm s^{-1}) average quadrupole splitting. Estimated errors ≤ 0.02 mm s^{-1} for IS and QS.

S2.9. Magnetic Behaviour

Magnetic Measurements

The temperature-dependent susceptibility of polycrystalline samples under an applied field of 1000 Oe was measured in the range of 2-300 K. The data were then normalized for atomic mass and the diamagnetic correction applied using tabulated Pascal's constants.[6] An initial fit was carried out to the Curie Weiss model with an additional temperature independent background diamagnetism over the range 100 to 300 K, giving a Curie constant, C = 3.41(1) emu K mol^{-1}, which corresponds to g = 2.13. The Weiss constant, T_{CW} = –25.2(4) K, was moderately antiferromagnetic. The diamagnet correction was $\chi_0 = 5.5(3) \times 10^{-4}4$ emu mol^{-1}.

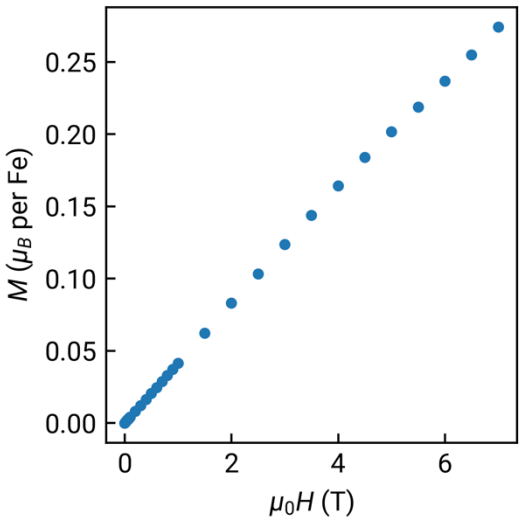

Figure S21. Magnetisation as a function of field at 1.8 K. Antiferromagnetic interactions are evinced by the low maximum measured magnetisation, M(μ_0H = 7 T) < gS.

Monte Carlo Simulations

We investigated the magnetic properties of these materials by Metropolis Monte Carlo simulations on a model of amorphous magnets, using methods outlined previously.[7] We generated our model from a 512 atom model of amorphous silicon with Si replaced by Fe^{II} generated using the Wooten-Winer-Weaire method (with complete 4-fold coordination)[8] with periodic boundary conditions.

We used a nearest neighbour antiferromagnetic Heisenberg Hamiltonian, $E = J\sum_{\langle i,j\rangle}\boldsymbol{S}_i \cdot \boldsymbol{S}_j$, where here $\mathbf{S}_i$ is a classical vector and summation is over all nearest-neighbour pairs. We explored models with 4x4x4, 3x3x3, 2x2x2 and 1x1x1 supercells, which found no evidence of boundary effects in the considered temperature regime for models larger than 1x1x1. We have therefore focussed on the 2x2x2 model. The models were gradually cooled from a high temperature (T/J = 100). A Monte Carlo "move" is an over-relaxation update followed by a random spin rotation. At each temperature, the number of proposed moves n_c needed to decorrelate the supercell was estimated; simulations were typically run for $10n_c$ for equilibration followed by 100 for measurement. It was possible to decorrelate the model at all temperatures studied in this work.

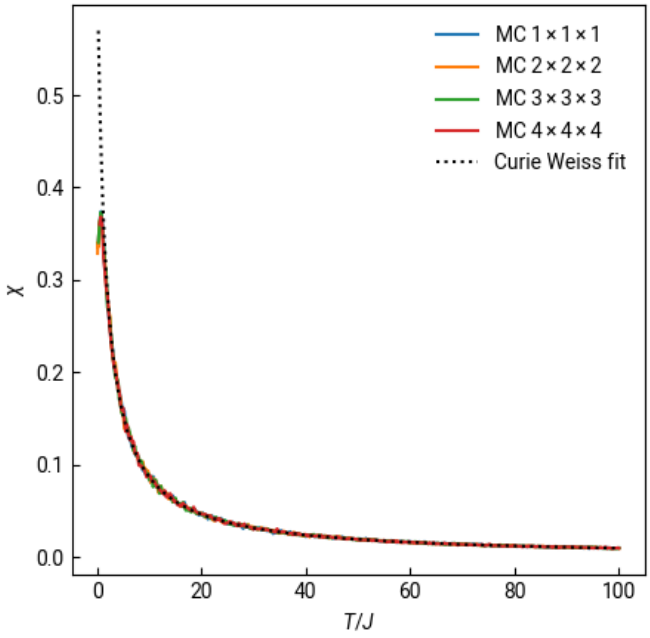

Figure S22. Simulated Monte Carlo susceptibility as a function of temperature for different supercell sizes.

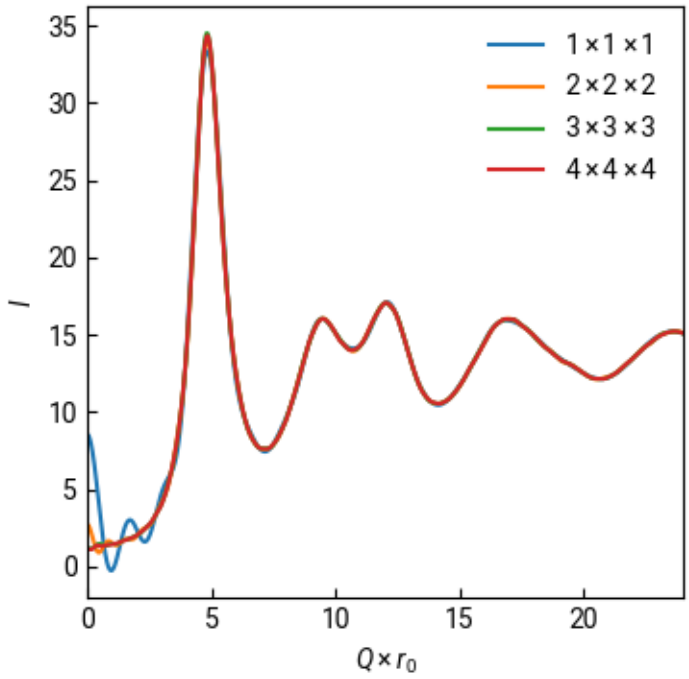

Figure S23. Simulated Monte Carlo neutron scattering diffraction pattern for four different supercell sizes.

To compare our model to the experimental data, we estimated the value of J from the experimentally determined Weiss constant, $J = -\frac{2}{3}T_{\mathrm{CW}} = 16.6$ K, and used the experimentally determined values of g and the diamagnetic correction χ_0. We included no additional free parameters. A deviation is noted at low temperatures, which perhaps relates to the finite size of the simulation box. Indeed, we note that calculation of the correlation length from the width of the FSDP suggests that the correlation length begins to approach the box size, implying interactions between periodic replicas may be significant even for this large cell. Investigation of the Monte Carlo derived spin and quadrupole correlation functions showed a broadly exponential decay consistent, and the local spin correlations show random spin orientations (ESI Fig. S27) consistent with speromagnetism.

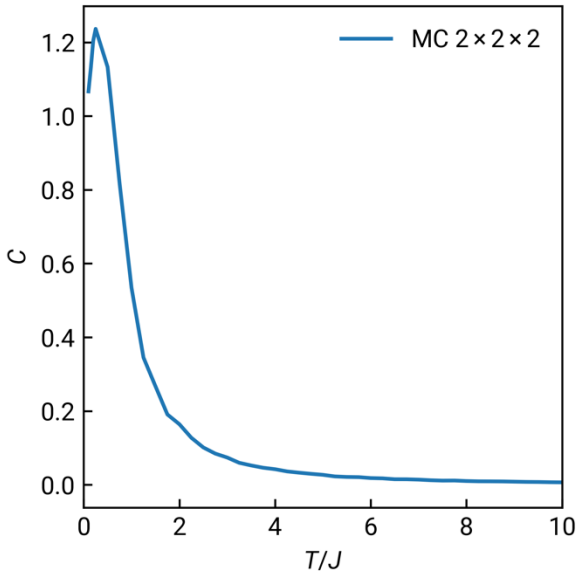

Figure S24. Monte Carlo simulated heat capacity for the simulations described in the main text.

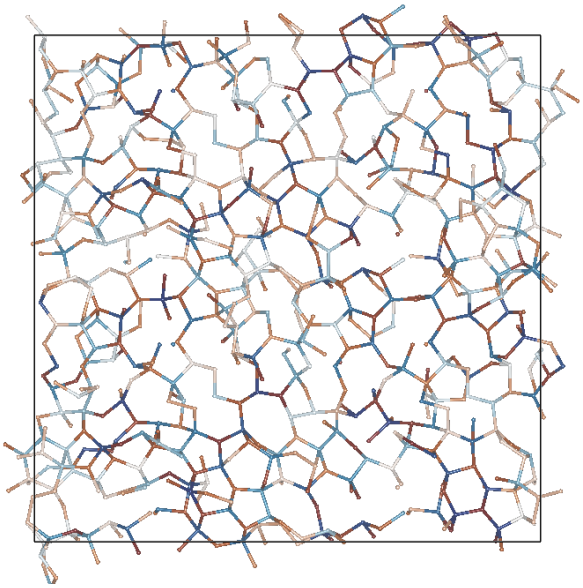

Figure S25. A section of the Monte Carlo simulation at $J/T_{sim} = 0.1$ coloured by S_z. Atoms with blue have $S_z = 1$, atoms in dark red $S_z = -1$, and white atoms have $S_z = 0$.

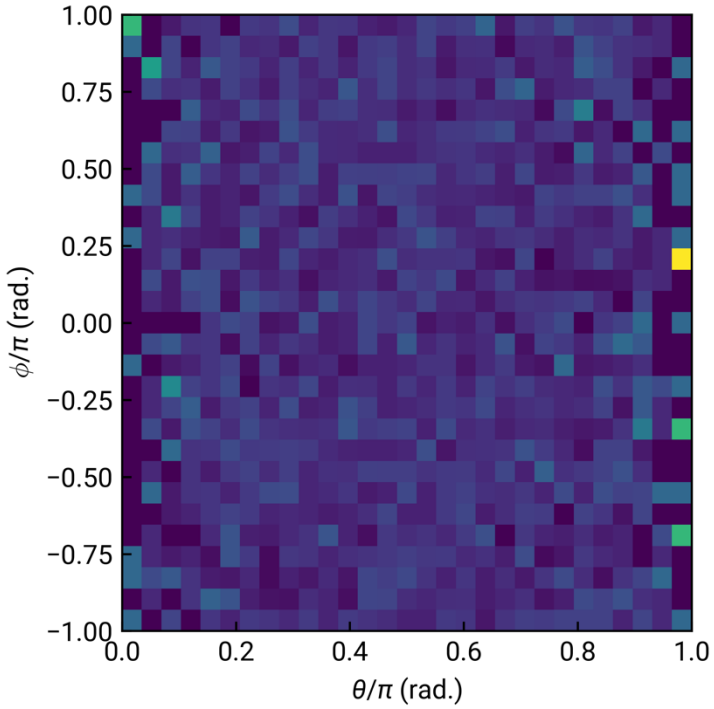

Figure S26. Angular spin distribution plot $J/T_{\text{sim}} = 0.1$ shows no clear spin direction preferences.

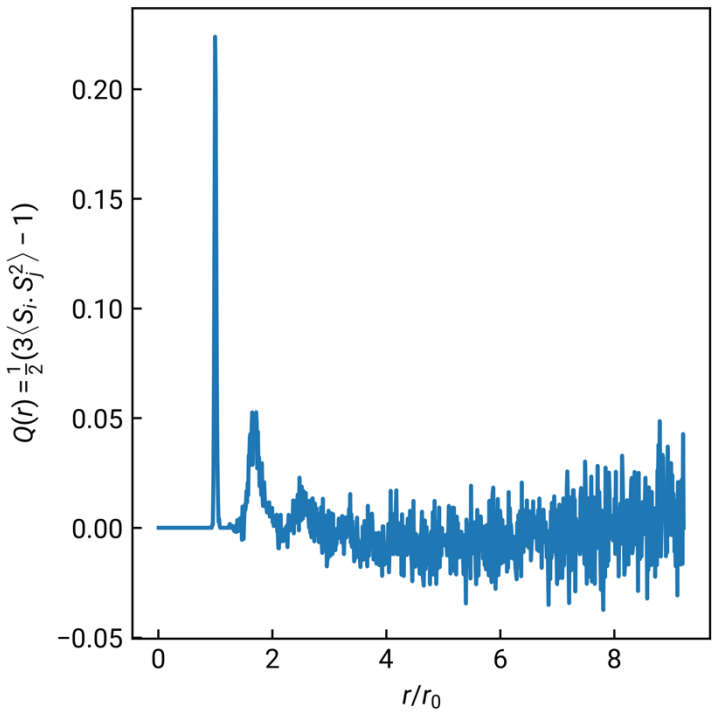

Figure S27. Quadrupole radial distribution function shows broadly exponential decay.

Neutron Scattering Analysis

To isolate the magnetic component of the neutron diffraction data, we subtracted the highest temperature dataset (T = 100 K) from each other dataset to remove the nuclear scattering. This temperature subtraction will be incomplete, as the large differences in temperature mean that the nuclear scattering will not cancel completely due to thermal expansion, changes in the atomic displacement parameters and thermal diffuse scattering. As the material is amorphous it lacks Bragg peaks, and so we were not able to use the nuclear scattering to put the magnetic scattering on an absolute scale.

We calculated the predicted magnetic neutron scattering from our Monte Carlo simulations using the tabulated Fe^{II} form factor. To compare directly with experiment, it was necessary to include three additional parameters to account for the above issues: an overall scale, a constant offset and a linear in Q offset. These parameters were fitted to the lowest temperature dataset (T = 1.8 K) and then fixed for the other three subtracted datasets. We used the exchange constant J determined from the Curie Weiss analysis described above to select the Monte Carlo simulation most appropriate for each of our datasets. We found that the lowest temperature measurement (1.8 K) had significantly broader peaks than the expected simulation temperature (T_{sim}/J = 0.1) and that the data were better represented by T_{sim}/J = 0.75 (T = 13 K). This is likely due to some combination of broadening due to the structural disorder, and the observed deviation between the WWW model simulations and the experimental susceptibility.

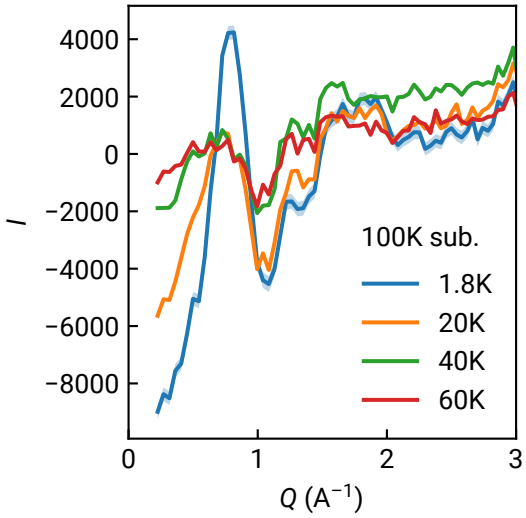

Figure S28. Plot of subtracted neutron scattering data as a function of temperature.

S2.10. Device characterization

For the deposition of the perovskite, centimeter-sized film of **dg-MUV-29** was used and secured with tape to ensure the proper vacuum deposition process (Figure S29). Figure S30 shows a SEM image of the **dg-MUV-29**/$MAPbI_3$ bilayer with the corresponding energy dispersive spectroscopy (EDS) maps. The SEM image shows a homogeneous perovskite surface coated on top of the MOF, as shown by the elemental maps of I/Pb (from the perovskite) and Fe (from **dg-MUV-29**). The current density vs. voltage curves were recorded with a Keithley 2612A SourceMeter and the devices were illuminated with a Wavelabs Sinus 70 LED solar simulator using a custom LabVIEW program. The light intensity was calibrated before every measurement using a calibrated Si reference diode.

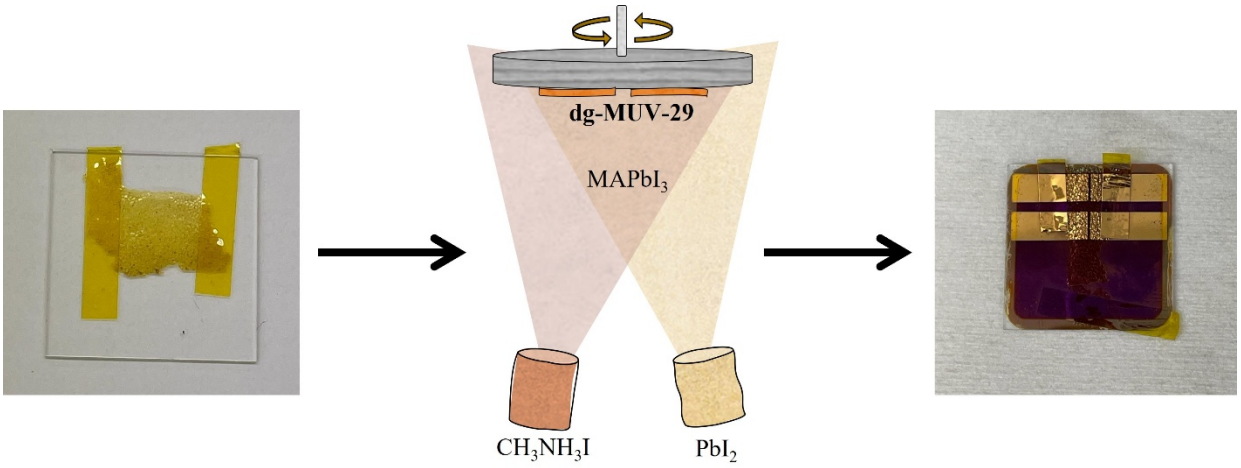

Figure S29. A centimeter-sized film **dg-MUV-29** used for vacuum deposition, where the perovskite layer was processed on the glass via co-sublimation of PbI_2 and MAI, followed by the evaporation of gold contacts using a shadow mask.

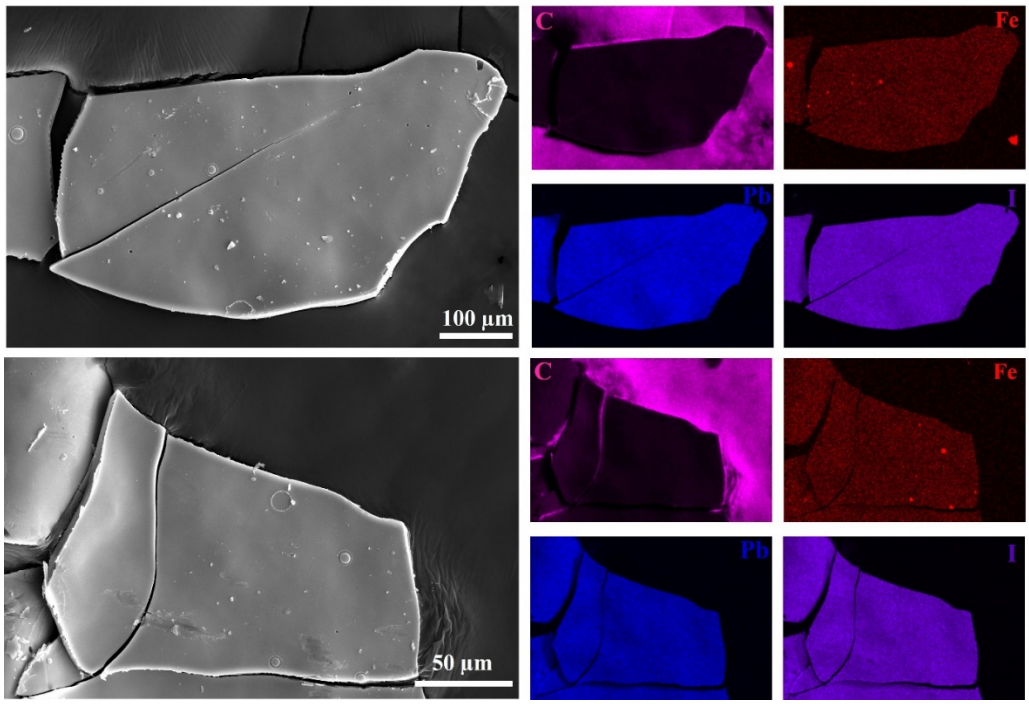

Figure S30. SEM and EDX mapping of the perovskite film deposited on **dg-MUV-29** glass.

S3. Synthesis and characterization of dg-MUV-29-X family

S3.1. Synthesis

All reagents were commercially available and used without further purification.

The incorporated amount of each ligand into the frameworks of **dg-MUV-29-NH_2, MUV-29-CH_3, MUV-29-Br** and **MUV-29-Cl.** was determined by ^{1}H NMR spectroscopy; (see Section S3.3).

Synthesis of **dg-MUV-29-NH_2 (dg-Fe(im)$_{1.56}$(5-NH_2-bim)$_{0.44}$).** Ferrocene (28 mg, 0.15 mmol) and a combination of imidazole (Him) (15.3 mg - 0.23 mmol) and 5-aminobenzimidazole (5-NH_2-bim) (9.9 mg - 0.07 mmol) were combined and sealed under vacuum in a layering tube (4 mm diameter). The mixture was heated at 300 °C for 6 hours, yielding to an orange glass. After cooling to room temperature, the layering tube was opened, and the unreacted precursors were extracted with acetonitrile, resulting in the isolation of orange glasses.

Synthesis of **dg-MUV-29-CH_3 (dg-Fe(im)$_{1.55}$(5-CH_3-bim)$_{0.45}$).** Ferrocene (28 mg, 0.15 mmol) and a combination of imidazole (Him) (15.3 mg - 0.23 mmol) and 5-methylbenzimidazole (5-CH_3-bim) (10.0 mg - 0.07 mmol) were combined and sealed under vacuum in a layering tube (4 mm diameter). The mixture was heated at 300 °C for 6 hours, yielding to an orange glass. After cooling to room temperature, the layering tube was opened, and the unreacted precursors were extracted with acetonitrile, resulting in the isolation of orange glasses.

Synthesis of **dg-MUV-29-Br (dg-Fe(im)$_{1.53}$(5-Br-bim)$_{0.47}$).** Ferrocene (28 mg, 0.15 mmol) and a combination of imidazole (Him) (15.3 mg - 0.23 mmol) and 5-bromobenzimidazole (5-Br-bim) (14.8 mg - 0.07 mmol) were combined and sealed under vacuum in a layering tube (4 mm diameter). The mixture was heated at 300°C for 6 hours, yielding to an orange glass. After cooling to room temperature, the layering tube was opened, and the unreacted precursors were extracted with acetonitrile, resulting in the isolation of orange glasses.

Synthesis of **dg-MUV-29-Cl (dg-Fe(im)$_{1.50}$(5-Cl-bim)$_{0.50}$).** Ferrocene (28 mg, 0.15 mmol) and a combination of imidazole (Him) (15.3 mg - 0.23 mmol) and 5-chlorobenzimidazole (5-Cl-bim) (11.4 mg - 0.07 mmol) were combined and sealed under vacuum in a layering tube (4 mm

diameter). The mixture was heated at 300 °C for 6 hours, yielding to an orange glass. After cooling to room temperature, the layering tube was opened, and the unreacted precursors were extracted with acetonitrile, resulting in the isolation of orange glasses.

Table S4. Applied masses and molar amounts of Him and Xbim in the reaction mixtures for the synthesis of **dg-MUV-29-X**. along with the *x* values used in synthesis and determined in the resulting framework (determined by ^{1}H NMR spectroscopy; see Section S3.3). In all cases, the experimental ratio was calculated using the signals from the protons of the imidazole ring, specifically those located at the C1 position (yellow and blue signals).

Material	Initial ratio (im^- : $Xbim^-$)	Experimental ratio (im^- : $Xbim^-$)
dg-MUV-29-NH_2	1.50 : 0.50	1.56 : 0.44
dg-MUV-29-CH_3		1.63 : 0.37
dg-MUV-29-Br		1.53 : 0.47
dg-MUV-29-Cl		1.51 : 0.49

S3.2. X-ray Powder Diffraction

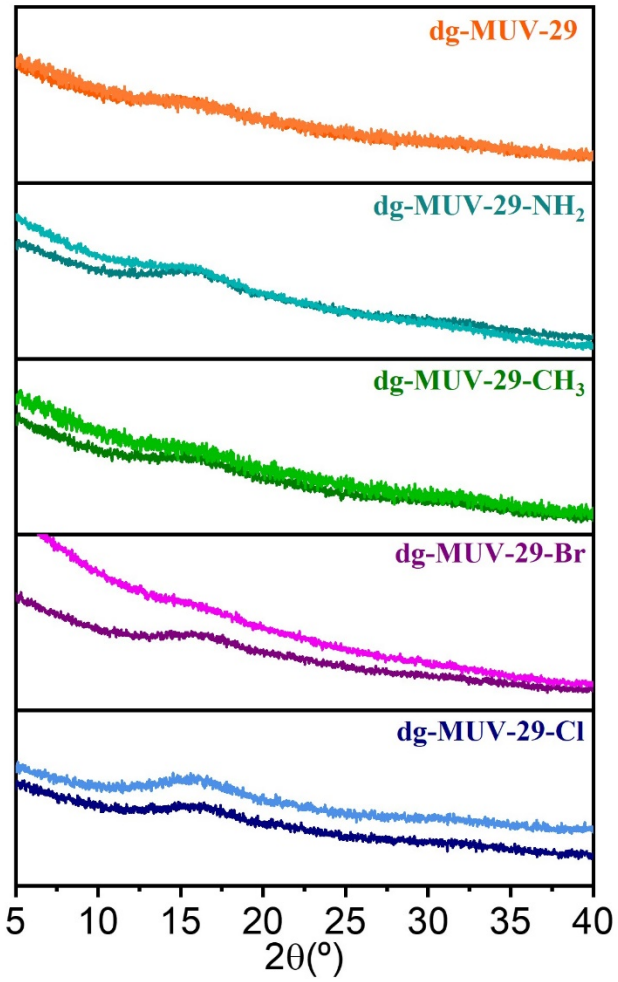

Figure S31. X-ray powder diffraction of **dg-MUV-29-X**. The dark line represents the material as-synthesized, while the lighter line corresponds to the X-ray powder diffraction of **dg-MUV-29-X** heated to the glass transition (300 ºC) and then cooled at a rate of 10 ºC min^{-1}. The absence of any Bragg diffraction peaks indicates no recrystallization.

S3.3. Nuclear Magnetic Resonance (NMR)

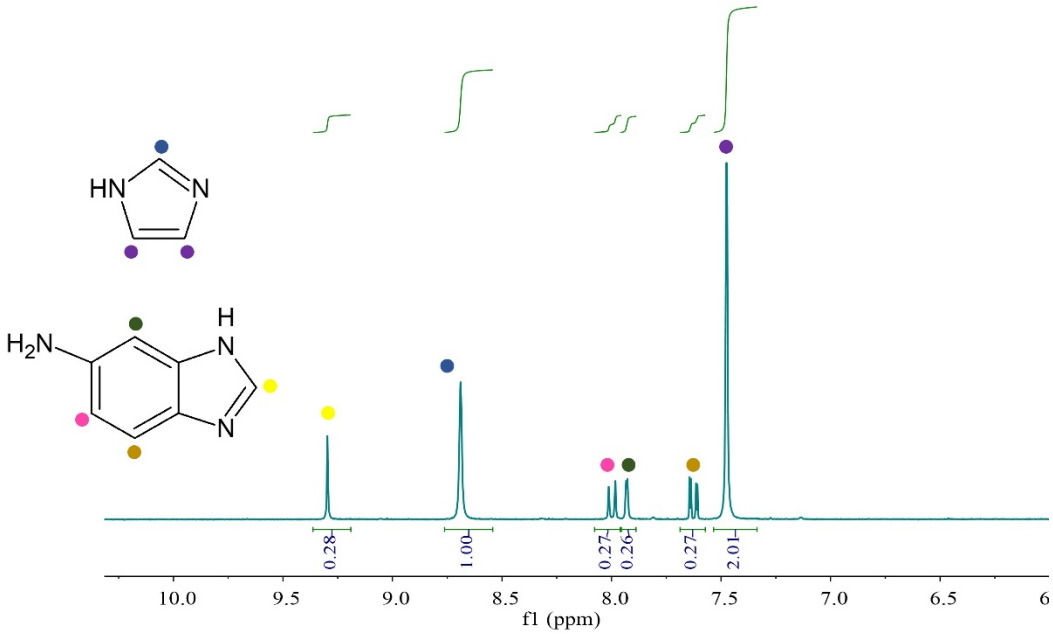

Figure S32. [1]H NMR spectra of the digested **dg-MUV-29-NH$_2$**. Colored circles help to localize the corresponding chemical shifts of the protons.

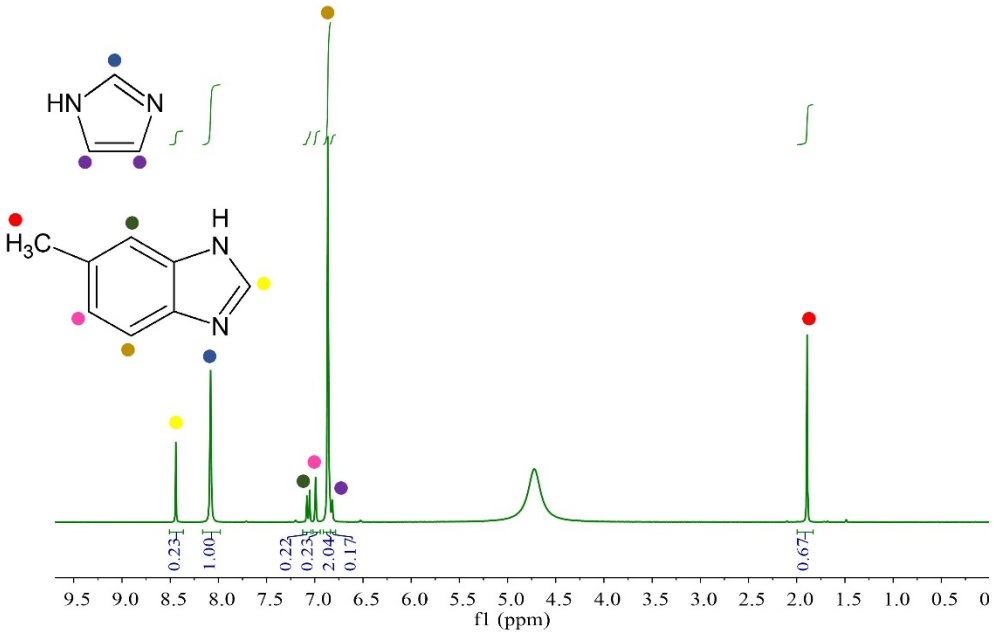

Figure S33. [1]H NMR spectra of the digested **dg-MUV-29-CH$_3$**. Colored circles help to localize the corresponding chemical shifts of the protons.

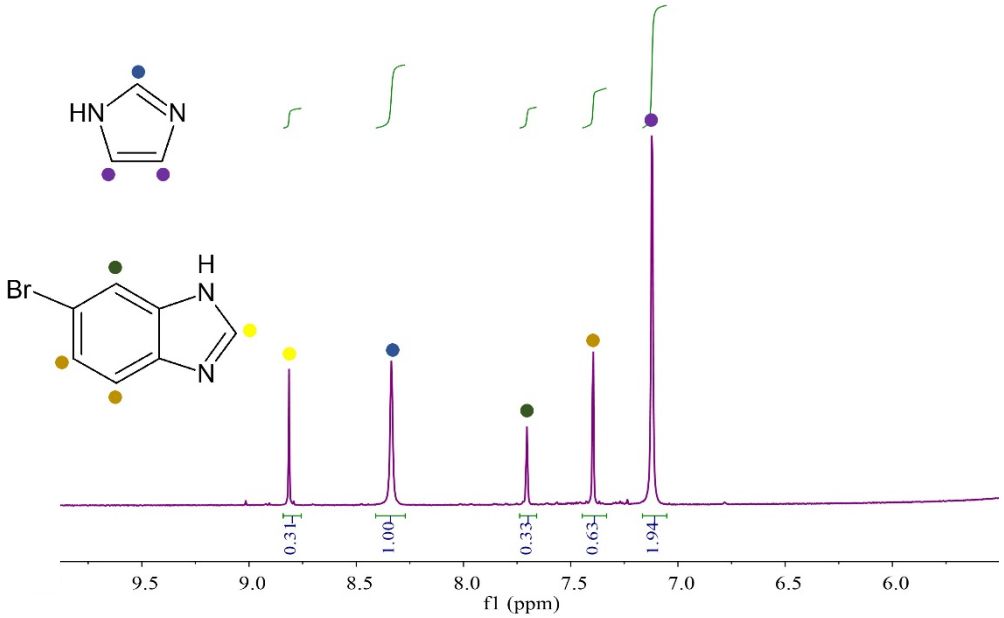

Figure S34. ^{1}H NMR spectra of the digested **dg-MUV-29-Br**. Colored circles help to localize the corresponding chemical shifts of the protons.

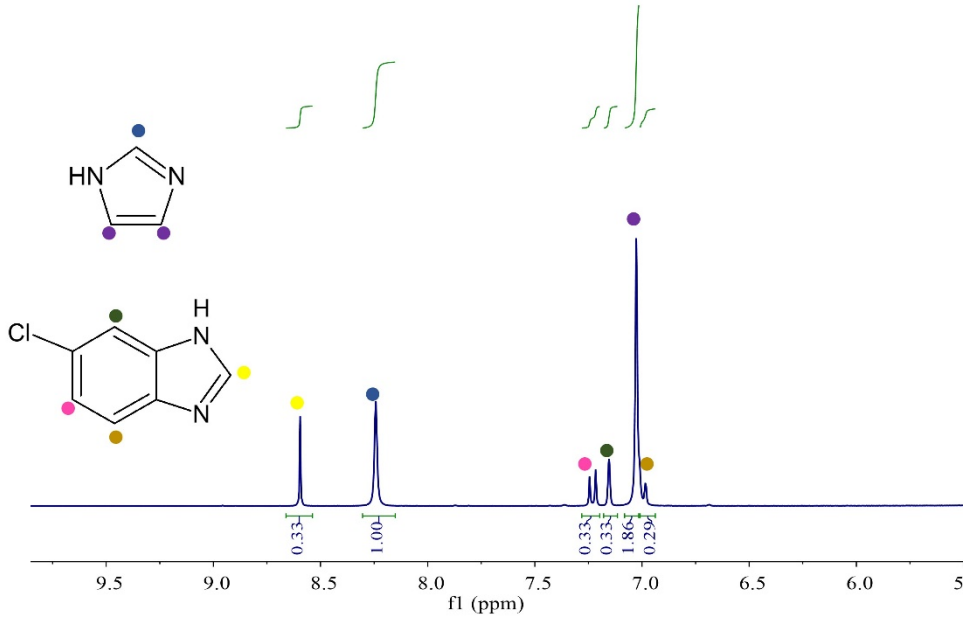

Figure S35. ^{1}H NMR spectra of the digested **dg-MUV-29-Cl**. Colored circles help to localize the corresponding chemical shifts of the protons.

S3.4. Differential Scanning Calorimetry (DSC)

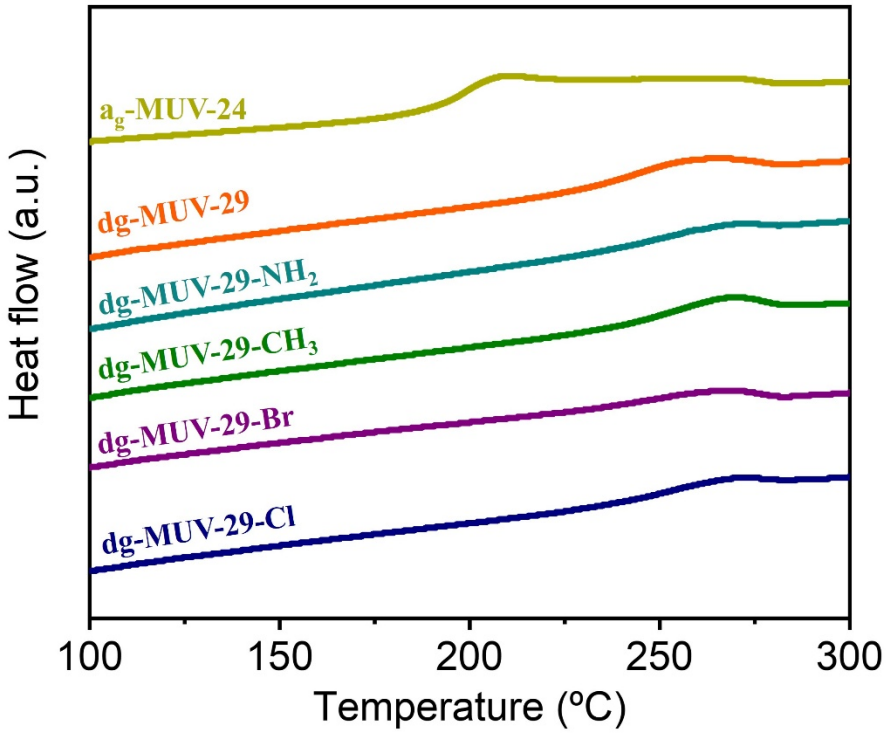

Material	Glass transition (ºC)
a_g-MUV-24	192
dg-MUV-29	228
dg-MUV-29-NH_2	247
dg-MUV-29-CH_3	245
dg-MUV-29-Br	243
dg-MUV-29-Cl	248

Figure S36. Top: DSC first upscan of **dg-MUV-29-X** family showing an increase in the glass transition temperature (T_g) compared to the **ag-MUV-24**. Below: Table displaying the glass transition values. The amount of bim incorporated in all cases corresponds to $x = 0.5$.

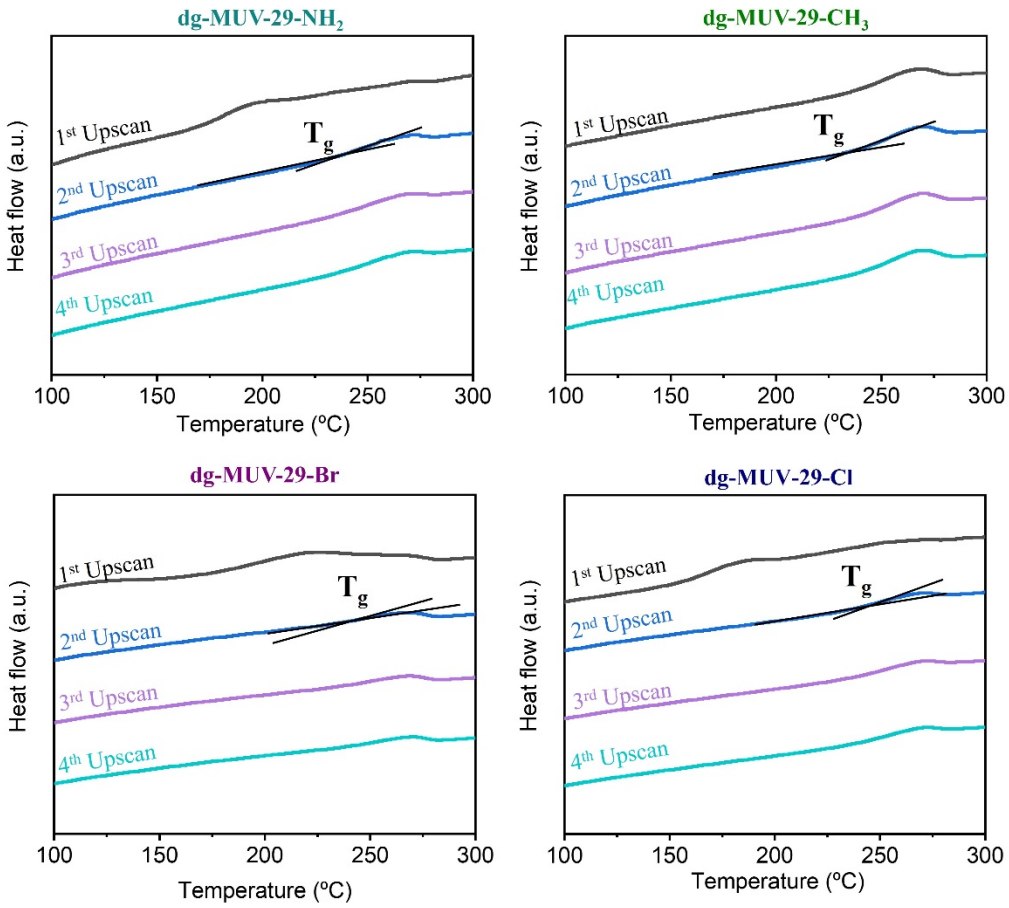

Figure S37. Successive DSC upscans of the **dg-MUV-29-X** family reveal a less defined step in the first upscan, corresponding to the activation of the material with the removal of some ligand molecules from the framework, same as in the case of **dg-MUV-29** with different amount of benzimidazole. The subsequent upscans demonstrate that the T_g is reversible, and the material remains stable throughout all cycles. The T_g intersection is shown only in the second upscan, as in the first upscan the transition is obscured by impurities. It is not displayed in the subsequent upscans to clearly demonstrate that the glass transition is maintained throughout the cycles. The amount of bim incorporated in all cases corresponds to $x = 0.5$.

S3.5. Polarized Light Microscopy

Figure S38. Optical images of different **dg-MUV-29-X** monolithic glass. Orange corresponds with **dg-MUV-29**. Blue corresponds with **dg-MUV-29-NH_2**. Green corresponds with **dg-MUV-29-CH_3**. Purple corresponds with **dg-MUV-29-Br**. Dark blue corresponds with **dg-MUV-29-Cl**. The amount of bim incorporated in all cases corresponds to $x = 0.5$.

S3.6. Scanning Electron Microscopy (SEM) and Energy Dispersive X-ray (EDX)

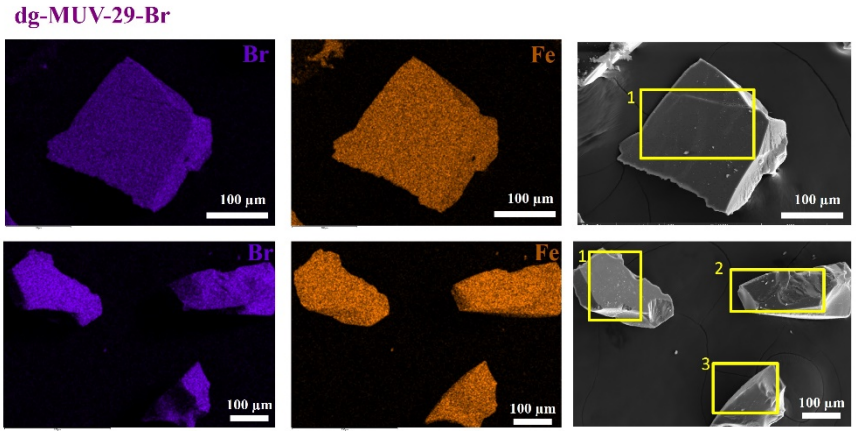

Tcal.	68.1%	31.9%
Position	%Fe	%Br
1	62.0	38.0

Position	%Fe	%Br
1	55.6	44.4
2	61.8	38.2
3	67.3	32.7

Figure S39. SEM and EDX mapping of various monoliths of **dg-MUV-29-Br**. The yellow rectangles indicate the areas where elemental analysis was performed to examine the ratio between iron and bromine ions (results shown in the tables on the right). This relation varies for each crystal. The amount of Br-bim incorporated corresponds to $x = 0.5$.

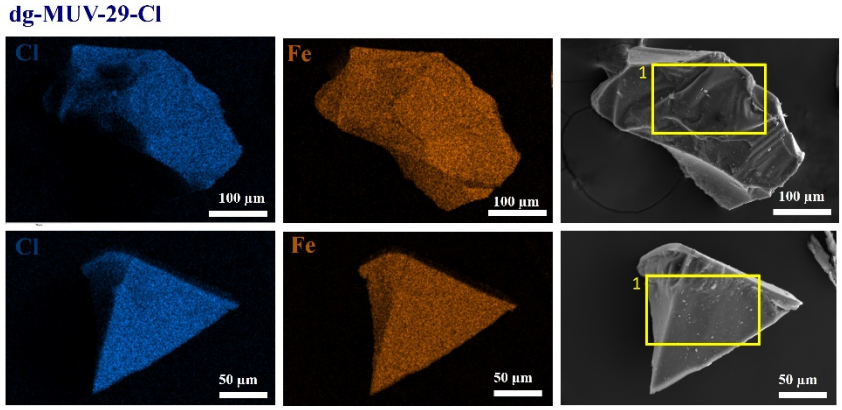

Tcal.	66.6%	33.3%
Position	%Fe	%Cl
1	88.6	21.4

Position	%Fe	%Cl
1	76.1	23.9

Figure S40. SEM and EDX mapping of various monoliths of **dg-MUV-29-Cl**. The yellow rectangles indicate the areas where elemental analysis was performed to examine the ratio between iron and chlorine ions (results shown in the tables on the right). This relation varies for each crystal. The amount of Cl-bim incorporated corresponds to $x = 0.5$.

S3.7. CO_2 adsorption

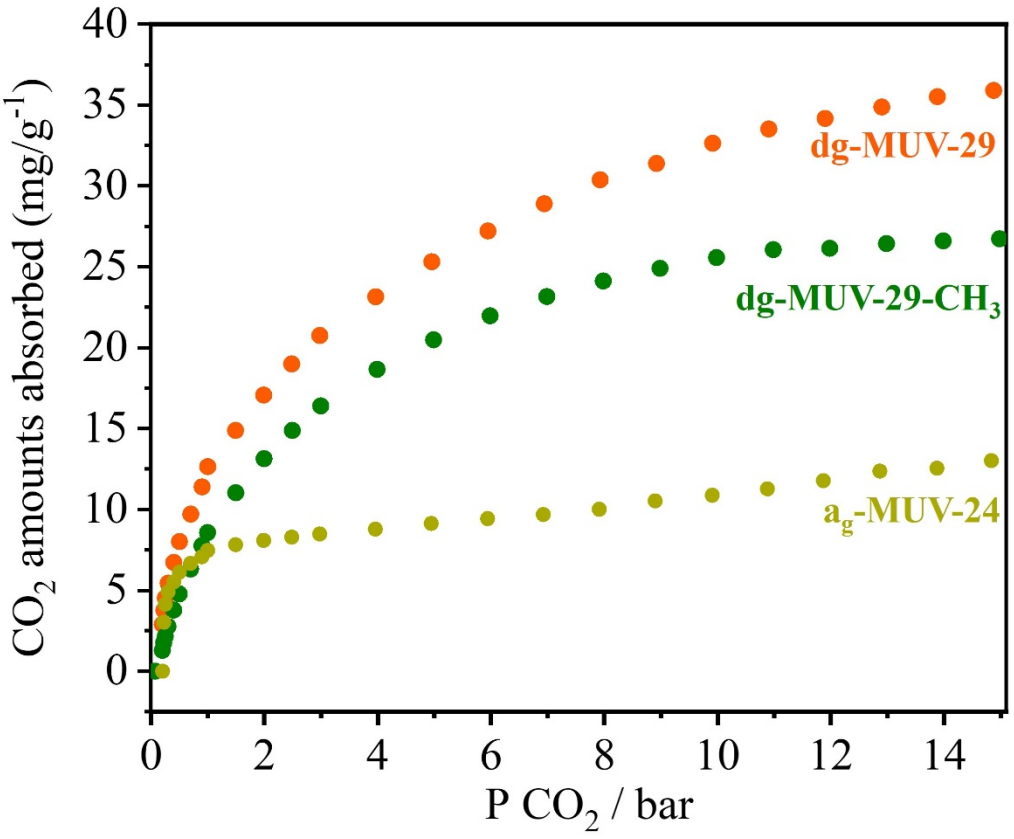

Figure S41. High pressure CO_2 gas sorption isotherms at 298K of **dg-MUV-29-X.**

S4. Synthesis and characterization of crystalline materials

S4.1. Synthesis

All reagents were commercially available and used without further purification.

Synthesis at low temperature conditions. Ferrocene (56 mg, 0.3 mmol) and a combination of imidazole (Him) and benzimidazole (Hbim) (0-0.60 mmol per reactant) with 8 different compositions: x = 0, 0.2, 0.4, 0.6, 0.8, 1.0, 1.5, 2.0) were combined and sealed under vacuum in a layering tube (4 mm diameter). The mixture was heated at 150°C for 4 days, yielding yellow crystals suitable for X-ray single-crystal diffraction. After cooling to room temperature, the layering tube was opened, and the unreacted precursors were extracted with acetonitrile, resulting in the isolation of orange crystals. The crystals obtained via this approach were analyzed via ^{1}H NMR and X-ray powder diffraction. Through X-ray diffraction, we observe the presence of one principal phase, known as **IMIDFE.** As the amount of benzimidazole increases, we observe the emergence of a second new phase. This previously unreported phase, which we have named **MUV-28** (MUV = Material of the University of Valencia), is based of imidazole and benzimidazole in varying ratios. This new phase crystallizes in the monoclinic $C2/m$ space group (a = 21.8385(17) Å, b = 18.5683(15) Å, c = 14.3092(11) Å, β = 108.224(9) º) and exhibits a 3D structure consisting exclusively of tetrahedral Fe^{II} centers coordinated by imidazolate ligands (Table S5 and Figure S55). The crystalline structure displays a random distribution between imidazolate and benzimidazolate ligands. Further addition of benzimidazole (x = 1.5) causes the appearance of another phase, **MUV-1**, which has been previously reported by our group. Also, differential scanning calorimetry (DSC) (Figure S58) shows a behavior quite similar to the pure iron counterpart, **MUV-24**. These results conclusively indicate that the nonporous network of **IMIDFE** is not incorporating benzimidazole on the structure and we are obtaining segregated phases of **IMIDFE, MUV-28** and **MUV-1**. This outcome is anticipated, as not all topologies can accommodate a bulkier ligand, similar to the case of the Zn derivative, being the only topology that can incorporate imidazole and benzimidazole the ***cag*** topology. This limitation motivated us to explore alternative synthetic conditions to successfully incorporate benzimidazole into the coordination network.

Table S5. Applied masses and molar amounts of Him and Hbim in the reaction mixtures for the synthesis of **IMIDFE**, **MUV-28** and **MUV-1**, along with the *x* values used in synthesis and determined in the resulting framework (determined by ^{1}H NMR spectroscopy; see Section S4.2) The purity of the phases was determined by X-ray powder diffraction, see section S4.4).

Prinicpal phase	Ratio : im^- : bim^-	x (expected)	x (found)
IMIDFE	1:0	0	0
IMIDFE	9:1	0.2	0.16
IMIDFE	4:1	0.4	0.21
IMIDFE	3:1	0.5	0.61
IMIDFE	2.33:1	0.6	0.63
MUV-28	1.5:1	0.8	0.73
MUV-28	1:1	1	0.98
MUV-1	1:2	1.5	1.79
MUV-1	0:1	2	2

Throughout this section, we will use *x* to represent the applied amount of benzimidazole to simplify the interpretation of the data, given the presence of a mixture of phases in many cases.

S4.2. Nuclear Magnetic Resonance (NMR)

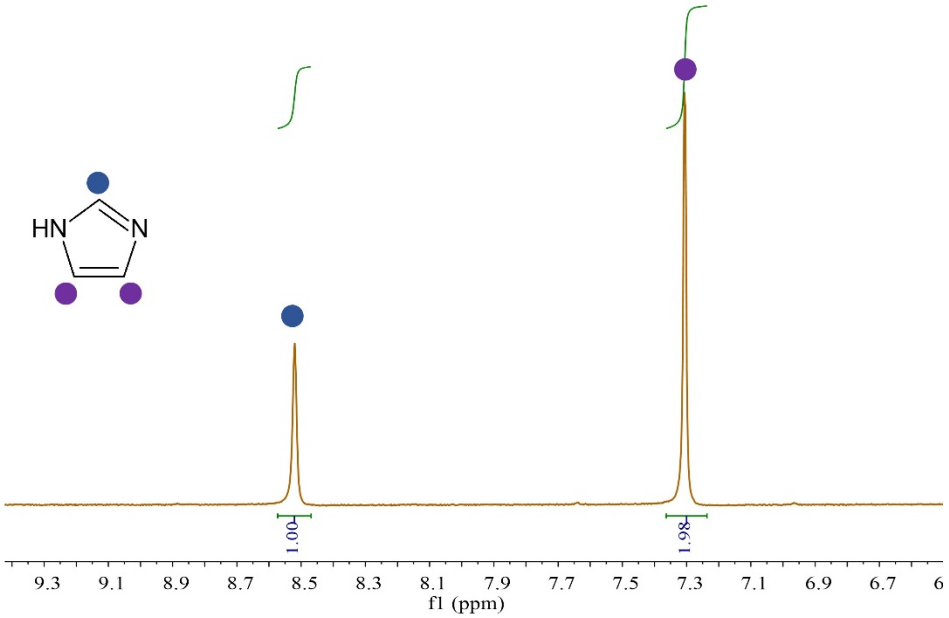

Figure S42. ^{1}H NMR spectra of the digested material with x = 0. Coloured circles help to localize the corresponding chemical shifts of the protons.

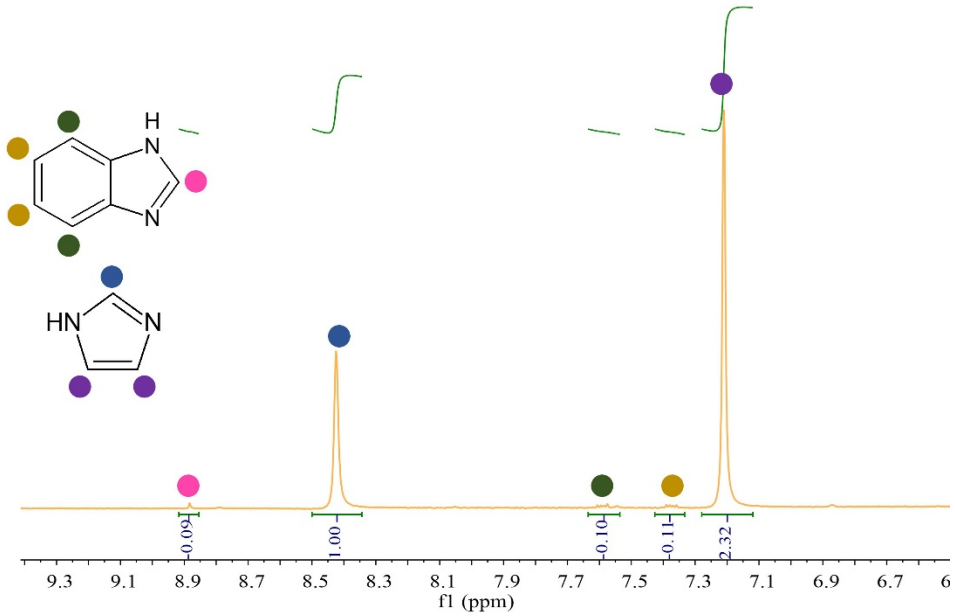

Figure S43. ^{1}H NMR spectra of the digested material with x = 0.2. Coloured circles help to localize the corresponding chemical shifts of the protons.

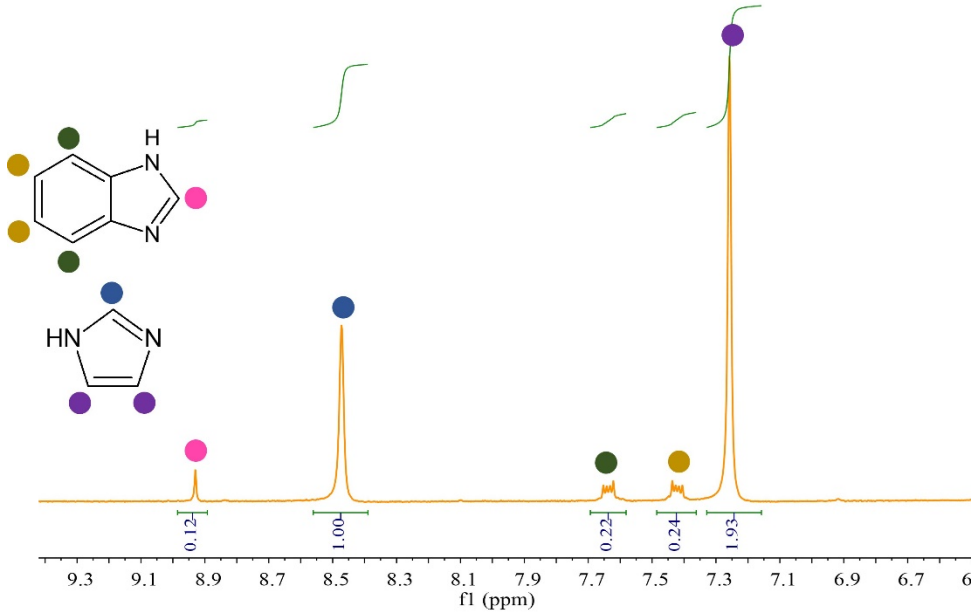

Figure S44. ^{1}H NMR spectra of the digested material with x = 0.4. Coloured circles help to localize the corresponding chemical shifts of the protons.

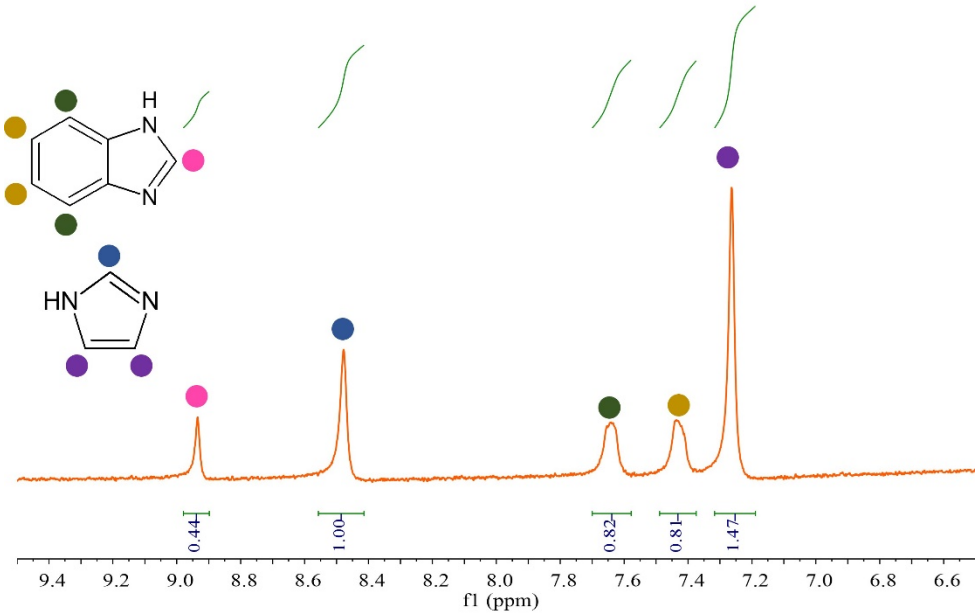

Figure S45. ^{1}H NMR spectra of the digested material with x = 0.5. Colored circles help to localize the corresponding chemical shifts of the protons.

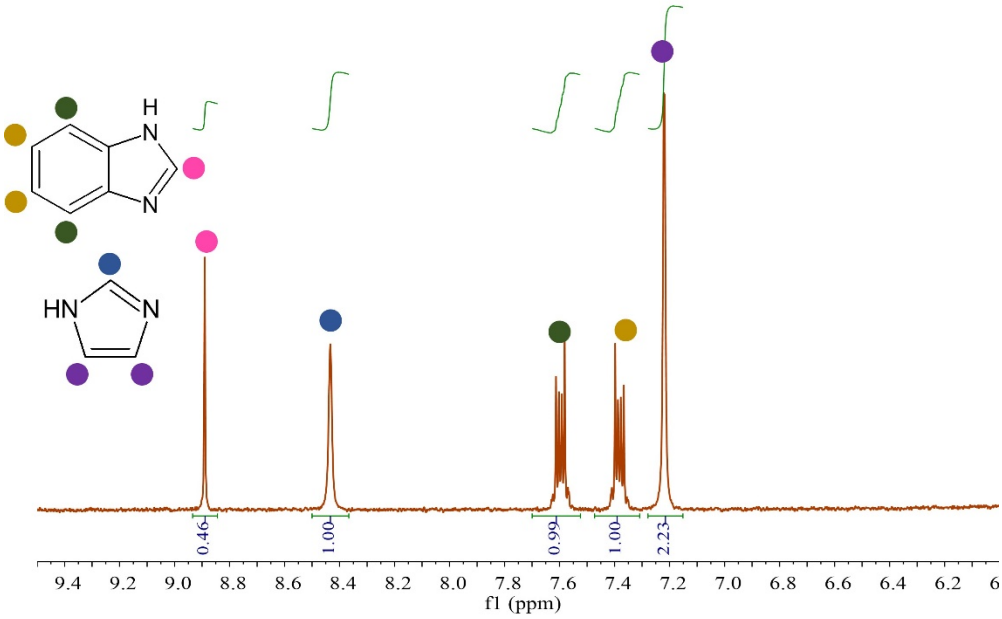

Figure S46. [1]H NMR spectra of the digested material with x = 0.6. Coloured circles help to localize the corresponding chemical shifts of the protons.

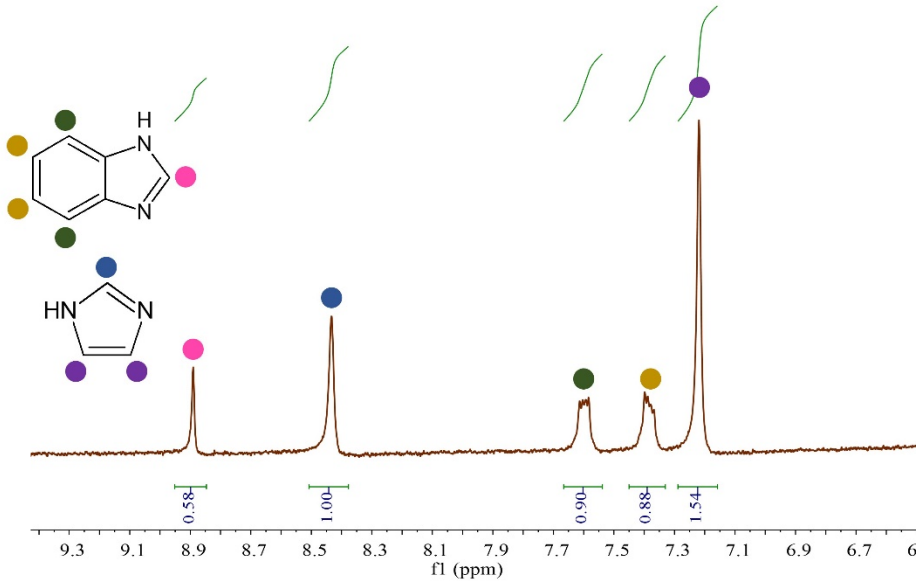

Figure S47. [1]H NMR spectra of the digested material with x = 0.8. (**MUV-28**) Coloured circles help to localize the corresponding chemical shifts of the protons.

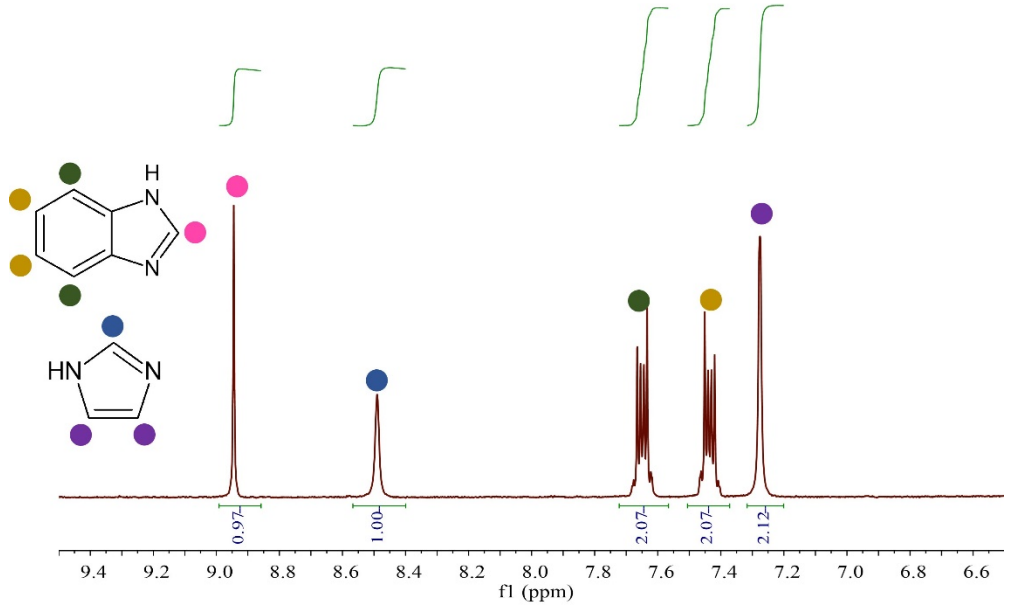

Figure S48. ^{1}H NMR spectra of the digested material with x = 1 (**MUV-28**). Coloured circles help to localize the corresponding chemical shifts of the protons.

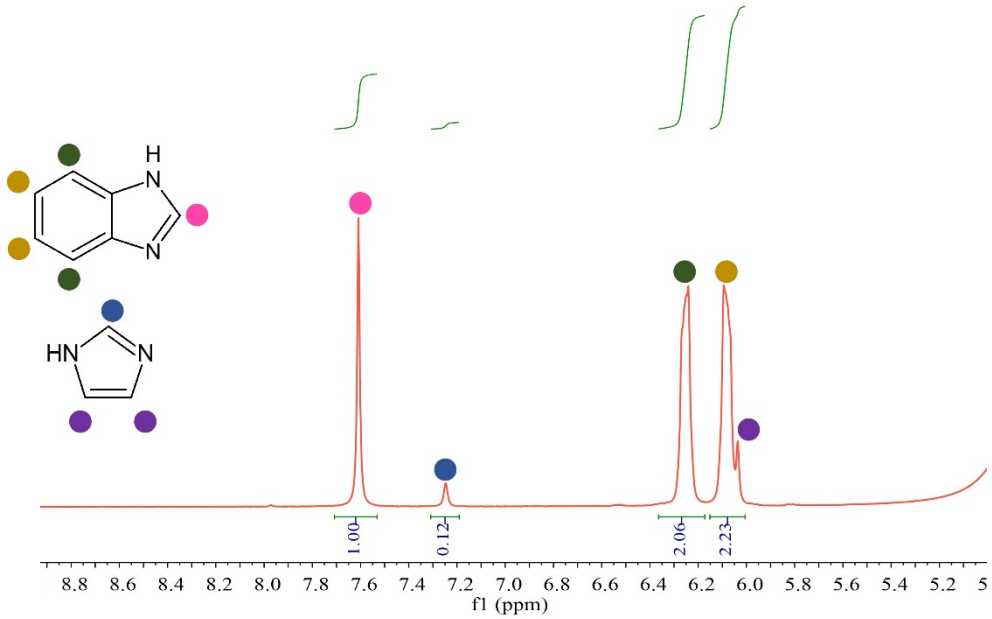

Figure S49. ^{1}H NMR spectra of the digested material with x = 1.5. Coloured circles help to localize the corresponding chemical shifts of the protons.

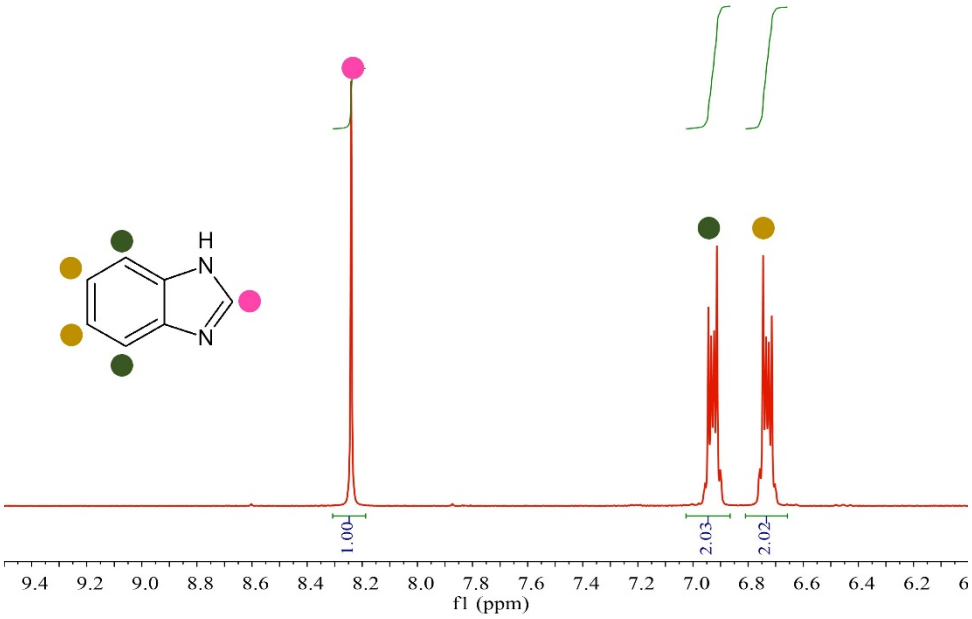

Figure S50. ^{1}H NMR spectra of the digested material with x = 2 (**MUV-1**). Coloured circles help to localize the corresponding chemical shifts of the protons.

S4.3. Single Crystal X-ray Diffraction (MUV-28)

A single crystal of **MUV-28** was mounted on glass fibers using a viscous hydrocarbon oil to coat the crystals and then transferred directly to the cold nitrogen stream for data collection. X-ray data were collected at 120 K on a DW rotating anode synergy R diffractometer with the (Cu-K_α) X-ray source (λ = 1. 54184 Å). Data were measured using the CrysAlisPro suite of programs. The program CrysAlisPro, Rigaku, was used for unit cell determinations and data reduction. Empirical absorption correction was performed using spherical harmonics, implemented in the SCALE3 ABSPACK scaling algorithm, based upon symmetry-equivalent reflections combined with measurements at different azimuthal angles. The crystal structure was solved and refined against all F^2 values using the SHELXL and Olex2 suite of programs.[9,10] Atomic displacement parameters of all non-hydrogen atoms were refined anisotropically. Hydrogen atoms were placed in calculated positions, refined using idealized geometries (riding model), and assigned fixed isotropic displacement parameters.

CCDC 2416331 contains the supplementary crystallographic data for this paper. These data can be obtained free of charge via www.ccdc.cam.ac.uk/conts/retrieving.html (or from the Cambridge Crystallographic Data Centre, 12 Union Road, Cambridge CB21EZ, UK; fax: (+44)1223-336-033; or deposit@ccdc.cam.ac.uk).

Table S6. Crystallographic information of compounds **MUV-28**

Identification code	**MUV-28**
Empirical formula	$C_{20}H_{16}Fe_2N_8$
Formula weight	480.11
Temperature/K	120(3)
Crystal system	monoclinic
Space group	*C*2/*m*
a/Å	21.8385(17)
b/Å	18.5683(15)
c/Å	14.3092(11)
α/°	90
β/°	108.224(9)
γ/°	90
Volume/Å^3	5511.4(8)
Z	8
ρ_{calc}/g·cm^{-3}	1.157
μ/mm^{-1}	8.592
F(000)	1952.0
Crystal size/mm^3	0.08 × 0.07 × 0.03
Radiation	Cu K_α (λ = 1.54184)
2Θ range for data collection/°	6.388 to 127.892
Index ranges	–25 ≤ h ≤ 24, –21 ≤ k ≤ 17, –15 ≤ l ≤ 16
Reflections collected	24946
Independent reflections	4631 [R_{int} = 0.1095, R_{sigma} = 0.0987]
Data/restraints/parameters	4631/0/ 288
Goodness-of-fit on F^2	0.987
Final R indexes [I>=2σ (I)]	R_1 = 0.0996 wR_2 = 0.2828
Final R indexes [all data]	R_1 = 0.1794 wR_2 = 0.3355
Largest diff. peak/hole / e Å^{-3}	0.67/–0.44

S4.4. X-ray Powder Diffraction

All materials were characterized by X-ray powder diffraction. Three distinct phases emerged depending on the proportion of the precursors Him and Hbim. When only Him was added, the phase obtained was **IMIDFE** ($Fe(im)_2$), as previously reported. Upon adding Hbim, another phase formed by $Fe(im)_1(bim)_1$, denoted as **MUV-28**, began to increase in intensity. This phase, previously unreported, became pure at a Hbim ratio of approximately 1:1. Further increasing the Hbim concentration as a ligand led to the appearance of another previously reported phase, **MUV-1**, formed exclusively by benzimidazole.

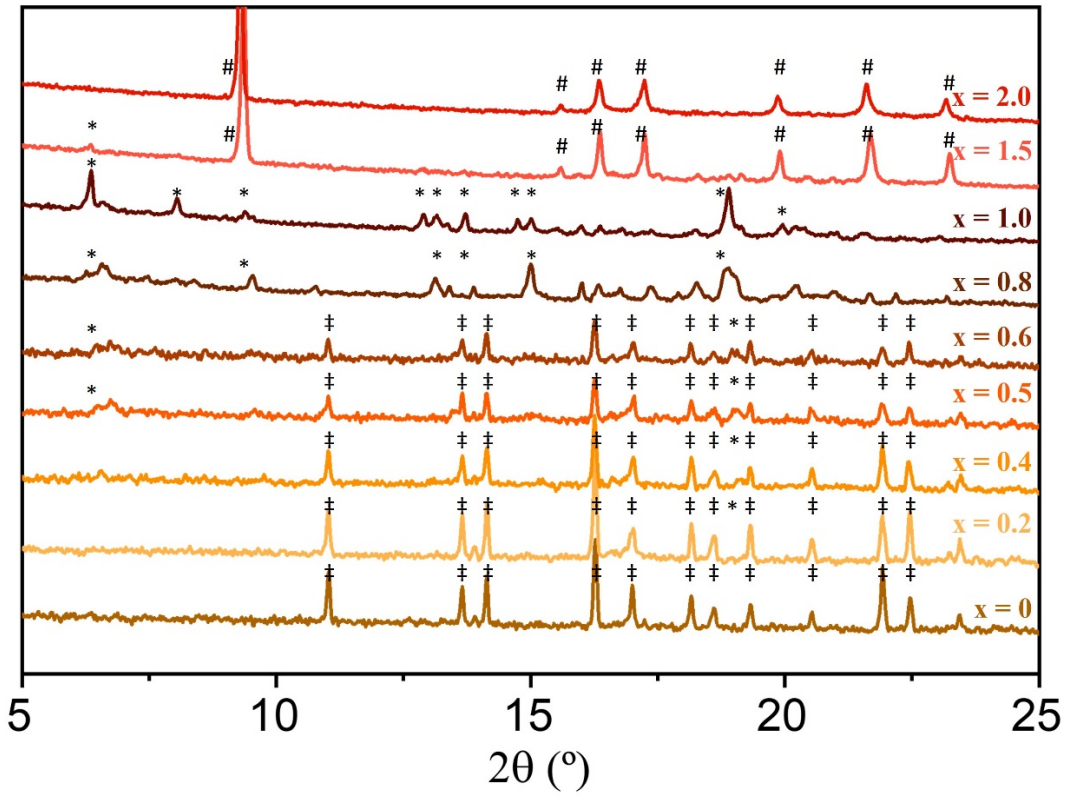

Figure S51. X-ray powder diffraction of the crystalline phases formed by varying molar amounts of Him and Hbim in the reaction mixtures, leading to the formation of **IMIDFE**, **MUV-28**, and **MUV-1**. The *x* values correspond to the amount of benzimidazole added during the synthesis.

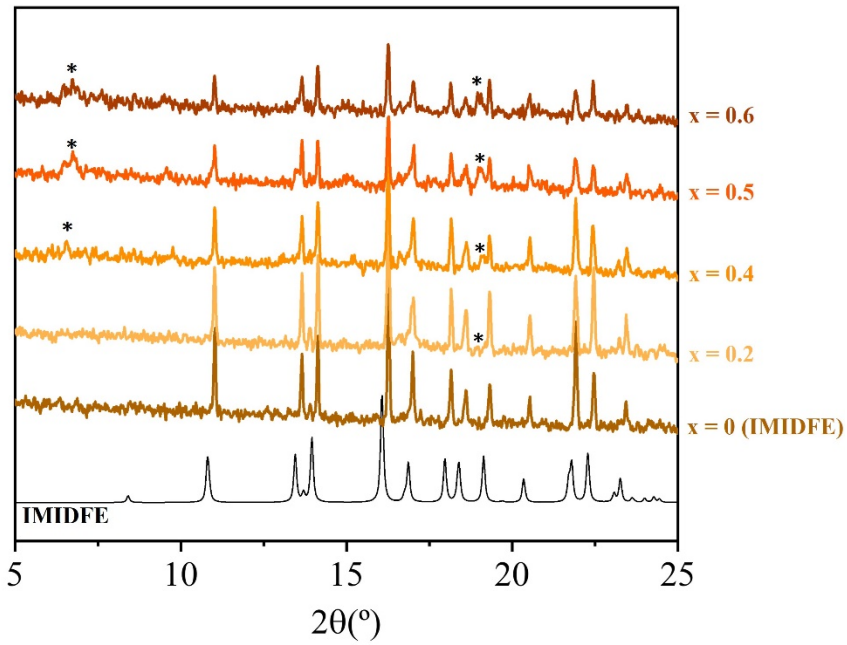

Figure S52. X-ray powder diffraction analysis of the material with $0 < x > 0.6$ reveals that the predominant phase is **IMIDFE**. However, the crystalline phase **MUV-28** ((marked with an asterisk) emerges with the increase of Hbim.

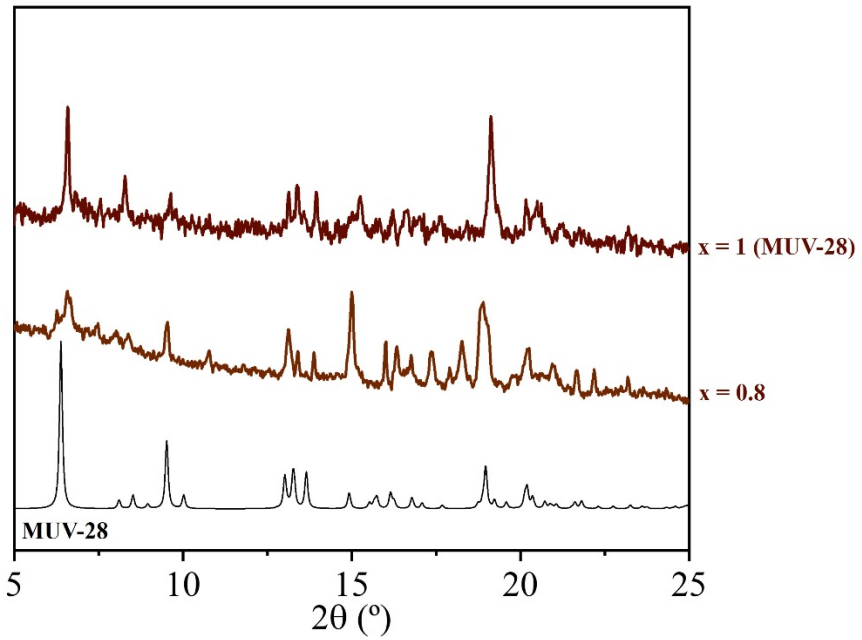

Figure S53. X-ray powder diffraction analysis of the material with $0.8 < x > 1$ reveals that the unique discernible phase is **MUV-28**.

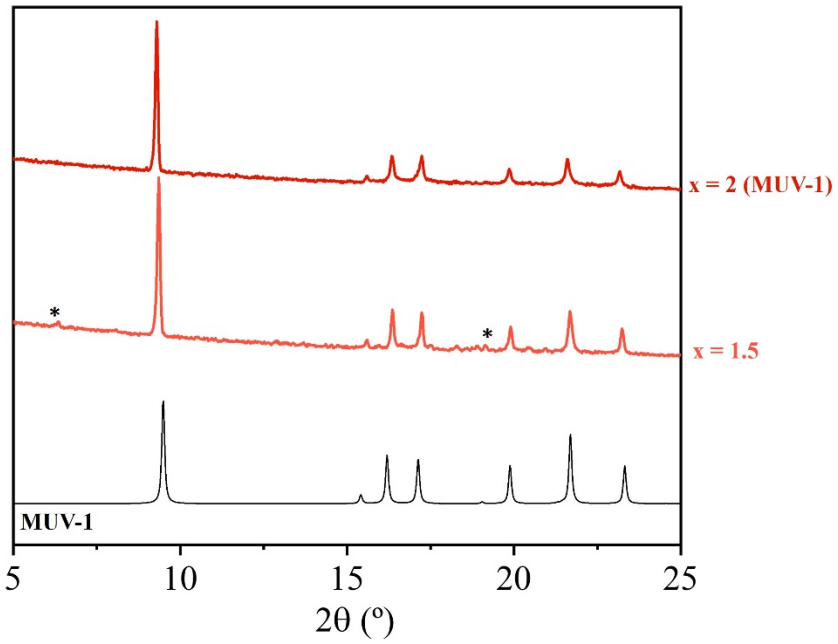

Figure S54. X-ray powder diffraction analysis of the material with $1.5 < x > 2$ reveals that the predominant phase is **MUV-1**. However, the crystalline phase **MUV-28** (marked with an asterisk) appears when the imidazole is added.

S4.5. Scheme of the synthesis protocols

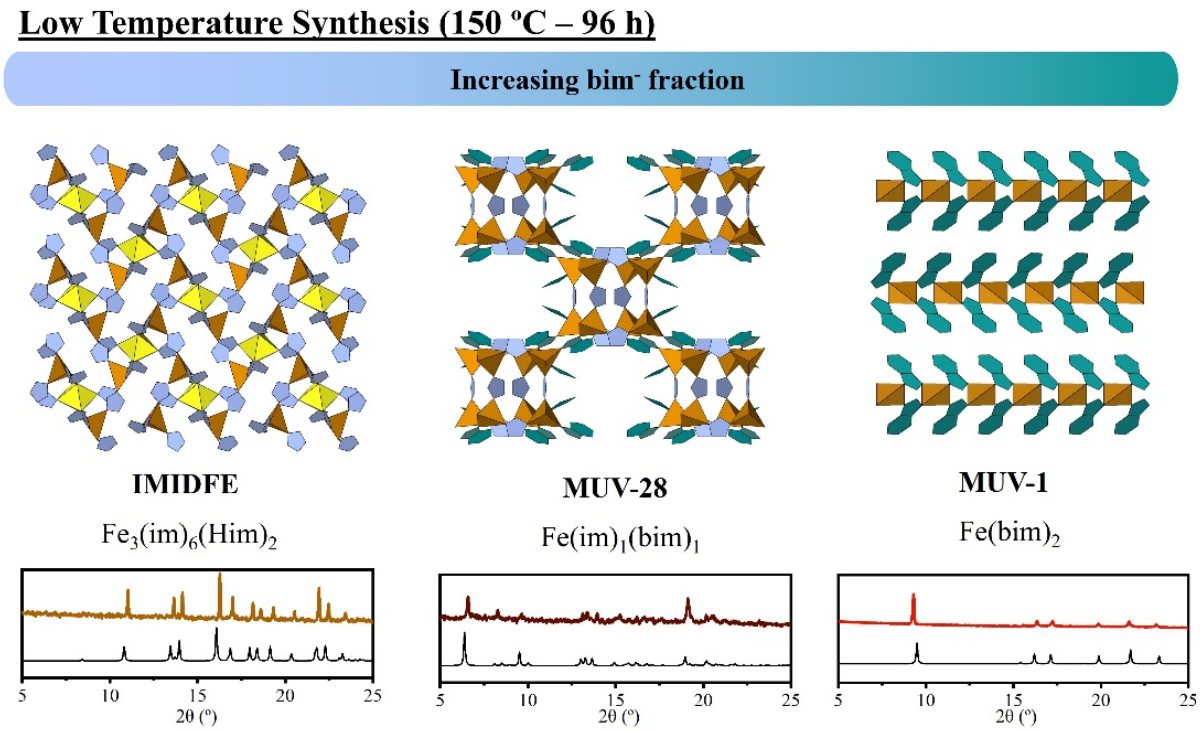

Figure S55. Schematic representation of the various compounds achievable through solvent-free synthesis using different protocols. By heating the sample at 150 ºC for 96 hours, **IMIDFE**, **MUV-28**, and **MUV-1** can be obtained by adjusting the amount of benzimidazole.

S4.6. Polarized Light Microscopy

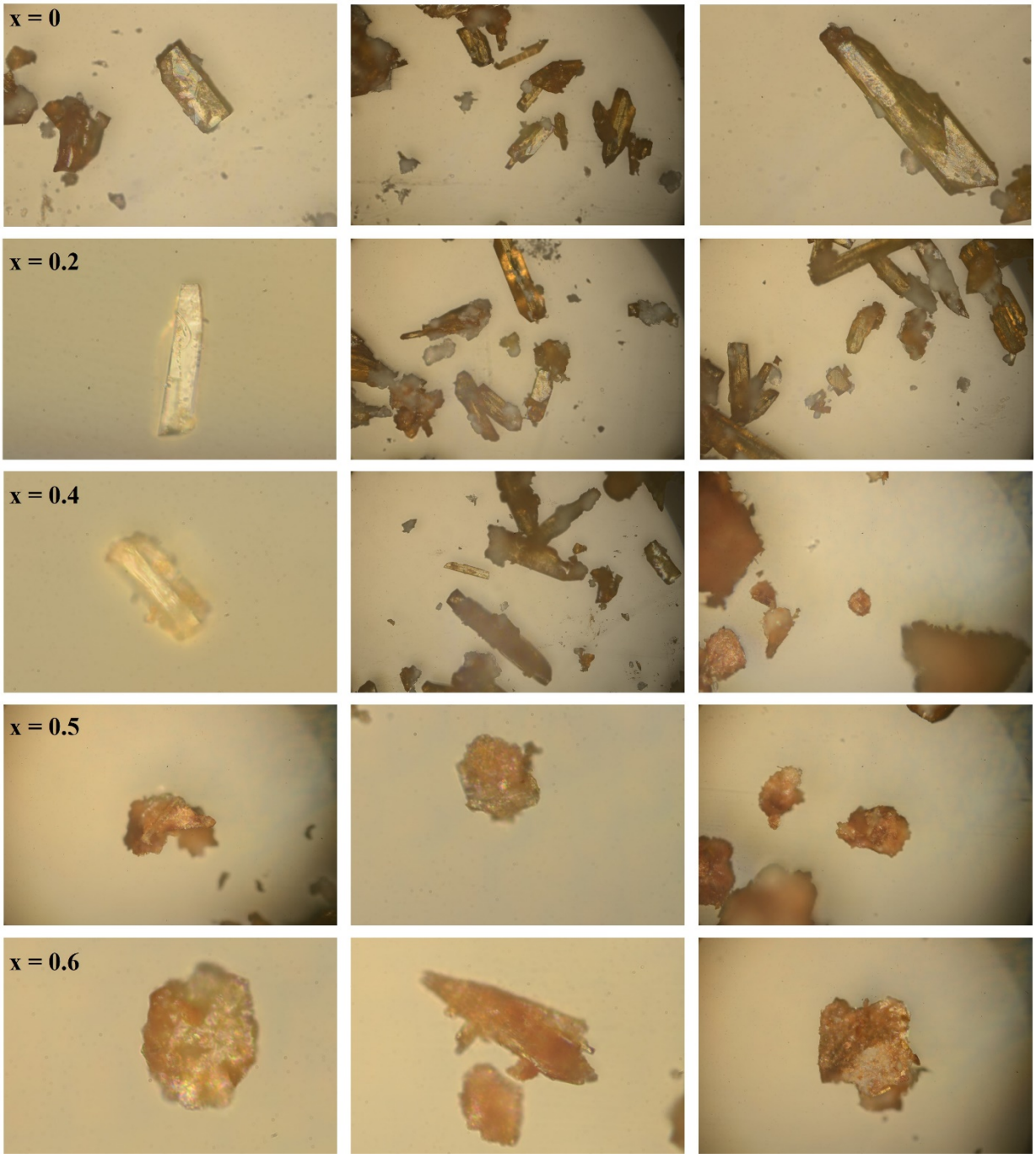

Figure S56. Optical images of crystals with $0 < x > 0.6$ revealed that, except in $Fe(im)_2$ where only **IMIDFE** crystals are present, a mixture of phases (**IMIDFE** and **MUV-28**) was observed.

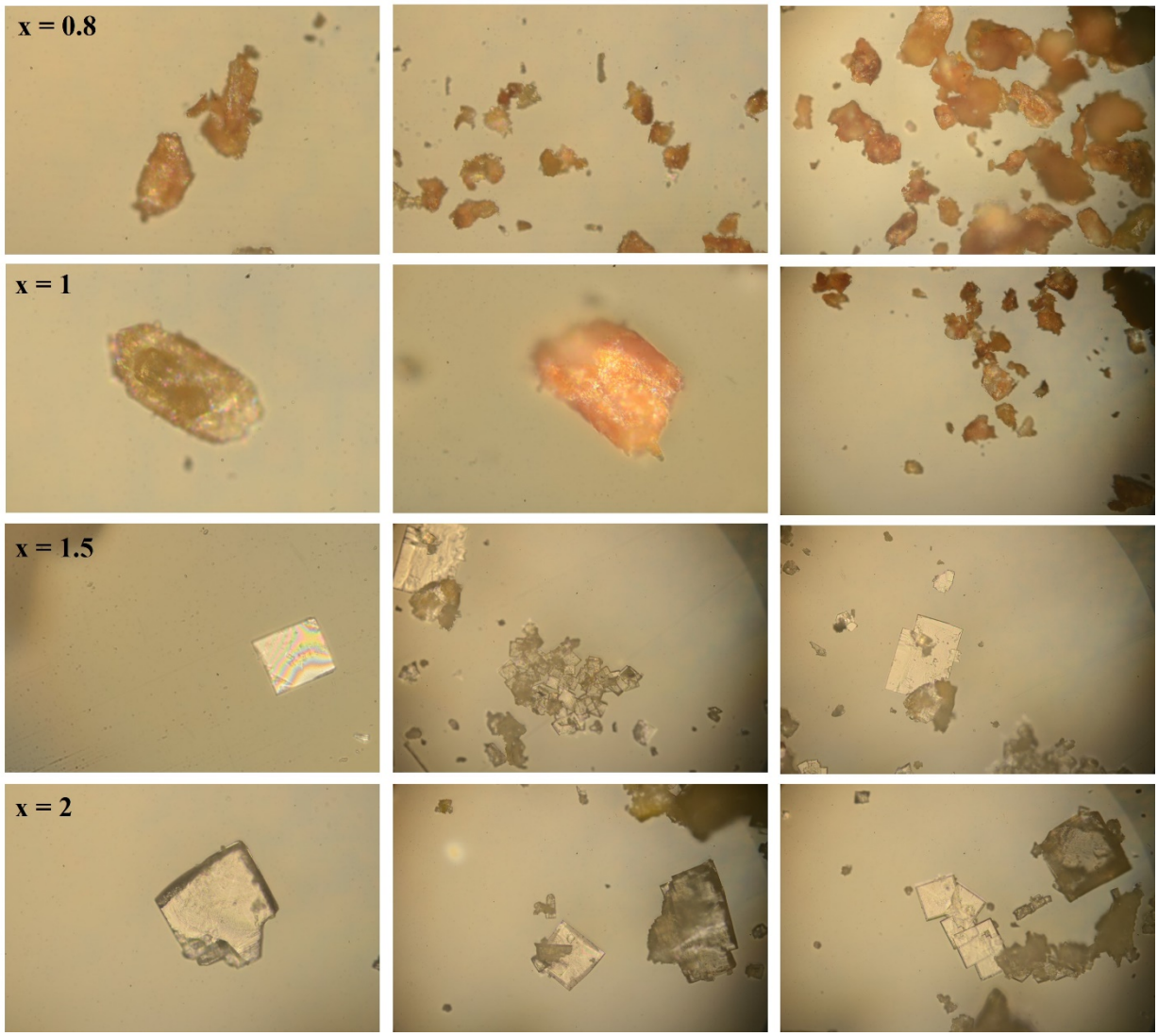

Figure S57. Optical images of crystals with $0.8 < x > 1$ corresponds with **MUV-28.** Optical images of crystals with $1.5 < x > 2$ corresponds with **MUV-1**.

S4.7. Differential Scanning Calorimetry (DSC)

The different samples were initially heated to 40 °C, followed by a 15-minute isotherm to stabilize the environment. Subsequently, the sample was heated to 500 °C at a rate of 10 °C min^{-1}. Upon reaching 500 °C, a 10-minute isotherm was performed to ensure a complete phase change. The sample was then cooled back to 40 °C at 10 °C min^{-1}. After, a second upscan under the same conditions was conducted to study the glass transition.

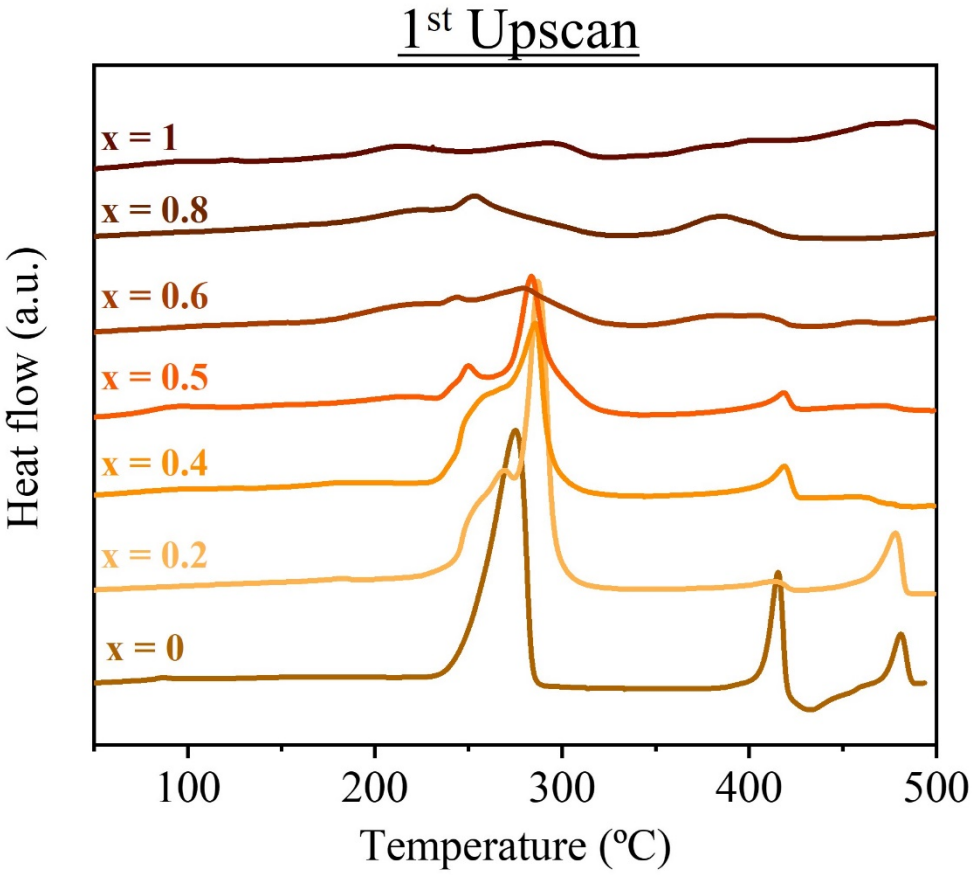

Figure S58. DSC first upscan of the materials with $0 < x > 1$ (no significant behavior is observed for $x > 0.98$). The phase transitions of $Fe(im)_2$ correspond to that previously reported for **IMIDFE**. These peaks decrease with increasing amounts of Hbim, indicating that **IMIDFE** undergoes melting and phase transitions, while **MUV-28** undergoes degradation.

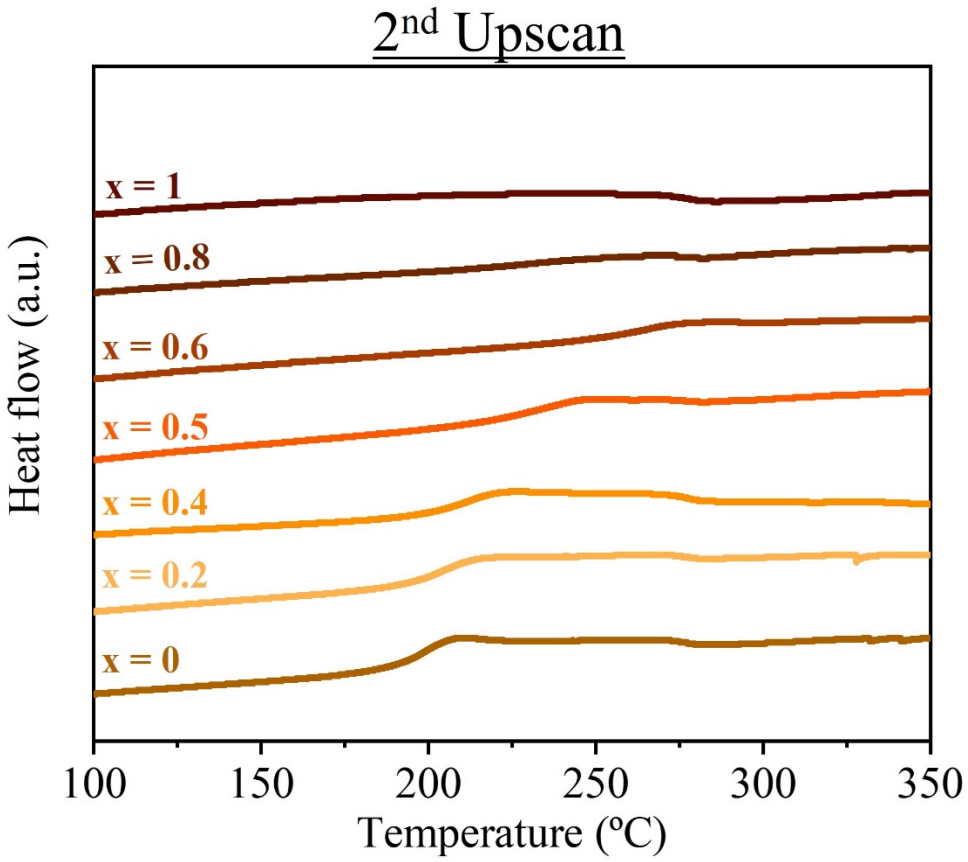

Figure S59. DSC second upscan of the materials with $0 < x > 0.98$. The glass transition is more pronounced when a higher proportion of the **IMIDFE** phase is present. This observation aligns with expectations since **IMIDFE** is the only material melting. On the contrary, when the phase is pure **MUV-28**, the glass transition is not observable.

S5. References

(1) León-Alcaide, L.; Christensen, R. S.; Keen, D. A.; Jordá, J. L.; Brotons-Alcázar, I.; Forment-Aliaga, A.; Mínguez Espallargas, G. Meltable, Glass-Forming, Iron Zeolitic Imidazolate Frameworks. *J. Am. Chem. Soc.* **2023**, *145*, 11258–11264.

(2) Greenwood, N. N.; Gibb, T. C. Mössbauer Spectroscopy. **1971**.

(3) Rettig, S. J.; Storr, A.; Summers, D. A.; Thompson, R. C.; Trotter, J. Transition Metal Azolates from Metallocenes. 2. Synthesis, X-Ray Structure, and Magnetic Properties of a Three-Dimensional Polymetallic Iron(II) Imidazolate Complex, a Low-Temperature Weak Ferromagnet. *J. Am. Chem. Soc.* **1997**, *119*, 8675–8680.

(4) Qi, Q.; O'Donnell, K.; Touchais, E.; Coey, J. M. D. Mössbauer Spectra and Magnetic Properties of Iron Nitrides. *Hyperf. Interact.* **1994**, *94*, 2067–2073.

(5) K. Ruebenbauer; T. Birchall. A Computer Programme for the Evaluation of Mössbauer Data. *Hyperf. Interac* **1979**, *7*, 125–133.

(6) Bain, G. A.; Berry, J. F. Diamagnetic Corrections and Pascal's Constants. *J. Chem. Educ.* **2008**, *85*, 532–536.

(7) Paddison, J. A. M.; Cliffe, M. J. Discovering Classical Spin Liquids by Topological Search of High Symmetry Nets. *ACS Cent. Sci.* **2024**. *10*, 1821–1828

(8) Wooten, F.; Winer, K.; Weaire, D. Computer Generation of Structural Models of Amorphous Si and Ge. *Phys. Rev. Lett.* **1985**, *54*, 1392.

(9) Dolomanov, O. V.; Bourhis, L. J.; Gildea, R. J.; Howard, J. A. K.; Puschmann, H. OLEX2: A Complete Structure Solution, Refinement and Analysis Program. *J. Appl. Cryst.* **2009**, *42*, 339–341.

(10) Sheldrick, G. M. SHELXT - Integrated Space-Group and Crystal-Structure Determination. *Acta Cryst. A Found. Adv.* **2015**, *71*, 3–8.